Scale interactions near the foothills of Himalayas during CAIPEEX

Thara V. Prabha,[1] Anandakumar Karipot,[2] D. Axisa,[3] B. Padma Kumari,[1]
R. S. Maheskumar,[1] M. Konwar,[1] J. R. Kulkarni,[1] and B. N. Goswami[1]

Received 28 August 2011; revised 4 April 2012; accepted 12 April 2012; published 24 May 2012.

[1] Scale interactions associated with small scale (<100 km) dynamics might play a crucial role in the distribution of aerosol in the Himalayan foothills region. Turbulence measurements from a horizontal flight path during Cloud Aerosol Interaction and Precipitation Enhancement EXperiment (CAIPEEX) are used to illustrate the scale interactions in the vertically sheared flow below the high-level subtropical westerly jet, which is important in the transport of pollution. Data analysis reveals the three dimensional property of large eddies that scale 10–12 km near the slopes, which could bring pollution from the valley to the Tibetan Plateau through a circulation adhering to the slopes. This circulation has a subsidence region away from the slopes and may also contribute to the buildup of pollution in elevated layers over the Plains. The vertical velocity and temperature spectra from research flight data showed clear indications of (−5/3) slope in the mesoscale range. The isotropic behavior of the velocity spectra was noticed for cloud-free traverses, while this behavior is distorted for cloudy conditions with the enhancement of energy at smaller scales as well as with low frequency gravity wave generation. A high-resolution cloud allowing model simulation over the flight path is used to examine the representation of these dynamical interactions in the numerical model. Based on the analysis of observational data and model inferences, a conceptual understanding of the flow in the region close to the foot hills and its role in the distribution of aerosol and cloud condensation nuclei is presented.

Citation: Prabha, T. V., A. Karipot, D. Axisa, B. P. Kumari, R. S. Maheskumar, M. Konwar, J. R. Kulkarni, and B. N. Goswami (2012), Scale interactions near the foothills of Himalayas during CAIPEEX, *J. Geophys. Res.*, *117*, D10203, doi:10.1029/2011JD016754.

1. Introduction

[2] Tibetan Plateau receives significant amount of radiation during the summer, leading to strong temperature contrast with the surrounding atmosphere. The Plateau also acts as a barrier on the atmospheric flows [*Murakami*, 1987] and generates a variety of atmospheric motions of contrasting time and space scales. The large-scale dynamics associated with this elevated Himalayan region and its influence on the Indian summer monsoon have been studied extensively [*Hahn and Manabe*, 1975; *Chakraborty et al.*, 2006; *Yanai and Wu*, 2006; *Wu et al.*, 2007; *Xavier and Goswami*, 2007; *Molnar et al.*, 2010].

[3] *Lau and Kim* [2006] and *Lau et al.* [2006, 2008] showed that absorbing aerosol may influence the South Asian monsoon through 'elevated heat pump' (EHP) mechanism. Their studies showed that dust and black carbon transported to higher altitude Himalayan regions and Tibetan Plateau enhanced rainfall in the Himalayan foothills. Consistent with the EHP hypothesis, the long-term upper tropospheric warming was observed over the western Himalayan region [*Gautam et al.*, 2009; *Prasad et al.*, 2009]. Black carbon aerosol in the boreal spring leads to wide spread warming and snowmelt in the Himalayan region [*Lau et al.*, 2010]. The clear-sky radiative forcing during this period due to dust and soot aerosol provides an elevated heat source over the Indo-Gangetic Plain [*Lau and Kim*, 2006; *Lau et al.*, 2006]. *Gautam et al.* [2009] showed that enhanced pre-monsoon warming over the Gangetic plains may also influence the monsoon circulation by increasing the land-sea thermal contrasts. The orographic and heterogeneous land-surface impacts on convective development and impact on the diurnal cycle of rainfall over the Himalayan region is also evident [*Liu et al.*, 2009]. A conceptual understanding of the convection and distribution of deep convective cores based on Tropical Rainfall Measuring Mission (TRMM) observations was provided by *Houze et al.* [2007]. Though there is good understanding of the large-scale (>100 km) dynamics in

[1]Indian Institute of Tropical Meteorology, Pune, India.
[2]Department of Atmospheric and Space Sciences, University of Pune, Pune, India.
[3]Research Applications Laboratory, National Center for Atmospheric Research, Boulder, Colorado, USA.

Corresponding author: T. V. Prabha, Indian Institute of Tropical Meteorology, Dr. Homi Bhabha Road, Pune 411008, India. (prabha.thara@gmail.com)

0148-0227/12/2011JD016754

this region, the small-scale dynamics (<100 km) and its significance in relation to aerosol distribution, cloud development and life cycle is not properly understood due to the scarcity of observations at that scale. A close relationship between the orography and the cloud cover in this region at scales of 5–150 km has been observed through satellite data analysis [*Barros et al.*, 2004], however this is not adequate to understand the dynamical interactions associated with the topographic, aerosol and cloud processes.

[4] There is rich knowledge on the aerosol physical and chemical properties [*Shrestha et al.*, 2000, 2002; *Carrico et al.*, 2003; *Stone et al.*, 2010; *Shrestha et al.*, 2010; *Decesari et al.*, 2010; *Brun et al.*, 2011; *Srivastava et al.*, 2011, 2012] and their diurnal variation [*Shrestha and Barros*, 2010] over the Himalayan region. The aerosol transport and redistribution to higher levels (up to 8 km) in this region has been associated with enhanced convection, and large scale orographic effects [*Liu et al.*, 2008] and influence from boundary layer flows such as mountain valley winds in localized observations [*Hindman and Upadhyay*, 2002; *Decesari et al.*, 2010]. *Shrestha and Barros* [2010] gives up-to-date account of studies that addressed the interaction between the topography and the aerosol distribution in the Himalayan region. Dust loading in the Indo Gangetic Plains during 2009 contributed to aerosol optical depths over 0.6 [*Gautam et al.*, 2011]. They reported a diurnal pattern of column integrated aerosol with afternoon peak from foothill to elevated mountain locations and attributed it to the increased upslope transport of pollutants – which they state 'likely represent large-scale lifting of absorbing aerosol along the elevated slopes during pre-monsoon season'.

[5] The development of clouds and their life cycle involves several microphysical and dynamical processes, which are intertwined. While in-cloud local temperature and humidity are regulated by updrafts/downdrafts within the clouds, large-scale dynamical effects are also important for microphysical characteristics. In this respect, non-local mixing of polluted air and its contribution to indirect effects of aerosol might play a crucial role in the cloud development over vertically sheared regions such as the Himalayan valley. Entrainment of outside air into the clouds and internal mixing further play a role in the cloud life cycle. Vertically sheared stably stratified flow and non-local entrainment may be assisted by vertical mixing in pockets where convective activity is supported by buoyant thermals, sometimes associated with biomass burning, which is an important source of aerosol [*Ramanathan and Crutzen*, 2003; *Ramanathan et al.*, 2005; *Lau et al.*, 2008]. Anthropogenic emissions particularly black carbon and sulfate aerosol from biomass burning, thermal plants, residential and vehicular activities are present throughout the year over this location [*Reddy and Venkataraman*, 2002a, 2002b]. Fire events that are typical over this region peak during the biomass burning season in April–May and have average burnt areas of 1129 sq. km, with the black carbon emissions of 431 Mg, per year [*Vadrevu et al.*, 2012]. They also note that fire induced radiative energy was maximum in the year 2009 over the Himalayan region of India and Nepal. The convective activity together with the strong buoyancy and turbulence created by active fires is able to carry biomass burning products to higher altitudes [*Folkins et al.*, 1997; *Chan et al.*, 2003; *Vadrevu et al.*, 2012]. However, over the Himalayan region, CALIPSO images repeatedly show high aerosol concentrations in the lowest 5 km layer and very low concentrations reaching the Tibetan plateau [*Kuhlmann and Quaas*, 2010]. *Liu et al.* [2008] also did not find transport across the region to Tibetan plateau. Strong spatial gradients in the aerosol optical depth is observed in the Moderate Resolution Imaging Spectroradiometer (MODIS) data across the region; covering the Gangetic valley and Tibetan plateau [*Shrestha and Barros*, 2010].

[6] The northwestern Himalaya appears to be a region where active interaction between aerosol, cloud microphysics, small scale turbulent processes and large scale dynamics play an important role in producing deep convective systems [*Houze et al.*, 2007]. For example, large concentrations of absorbing aerosol (local as well as transported) may produce elevated heat source and invigorate large-scale monsoon circulation [*Lau and Kim*, 2006]. Large incidence of fire can be seen in the MODIS fire counts. Also, very tall convective clouds (taller than 15 km) are found to occur over the region in large number [*Houze et al.*, 2007]. The sharp rise of the orography over the region also provides an ideal place for small-scale horizontal temperature gradient and buoyancy driven turbulence, which has not been investigated.

[7] Motivation for the current study stems from the fact that the scale interactions at scales less than 100 km near the Himalayas and how the aerosol or fire emission distribution influences the dynamics are not properly understood. The relevant boundary layer scales at which strong effects of different spatial scales take effect is not known. These aspects need to be investigated with the help of high-resolution spatial observations of aerosol, clouds, atmospheric parameters and numerical modeling.

[8] Recently, a major experiment named Cloud Aerosol Interaction and Precipitation Enhancement EXperiment (CAIPEEX) was conducted in India (see CAIPEEX science plan at http://www.tropmet.res.in/~caipeex/). Observations of middle and low-level clouds, and aerosol at several locations in India were carried out during Phase I of this experiment with an instrumented aircraft during May to September 2009 [*Prabha et al.*, 2011; *Kulkarni et al.*, 2012]. These first time cloud-aerosol-dynamics observations over India also included focused campaigns close to the Himalayan foothills region to investigate the aerosol and cloud distributions and their interrelationship with atmospheric dynamics.

[9] The main goal of the present study is to investigate the scale-interaction and their role in aerosol mixing and transport over the Himalayas and adjacent Ganges valley on the Indian side. The aircraft observations made in the region are used to study spectral and co-spectral characteristics. An attempt is also made to investigate the observational findings further with the help of a mesoscale model.

2. Data and Method

[10] Instrumented aircraft (Piper Cheyenne model PA-31 T) was used in Phase I of CAIPEEX. It could carry four persons, and climb up to a maximum altitude of 8.5 km, with a range 1200 nautical miles, and endurance of 5 h with scientific payload. The minimum rate of climb was 60.96 m per minute. CAIPEEX aircraft conducted several flights near the Himalayan region (originating at 32°17′N 75°39′E) during

Table 1. List of Instruments on Board the CAIPEEX Aircraft With Data Sampling Details[a]

Variable	Instrument	Range/Resolution
Cloud droplet spectra	DMT CDP	2–50 μm/1–2 μm
Cloud particle spectra	DMT CIP	25–1550 μm/25 μm
Liquid water content	DMT LWC-100	0–3 gm^{-3}/0.01 gm^{-3}
CCN	DMT CCN counter	0.5–10 μm (0.1 to 1.2% SS)/ 0.5 μm
Aerosol	PMS PCASP SPP 200	0.1–3 μm/0.02 μm
Temperature, Winds, Relative humidity	AIMMS	T: −30°C −50°C/ 0.01°C U, W: 0.01 ms^{-1}: RH: 0–100%/0.1%:
Altitude	Radar Altimeter	0–2000 ft/0.15 m

[a]PCASP is the Passive Cavity Aerosol Spectrometer Probe, CIP is the Cloud Imaging Probe, CDP is the Cloud Droplet Probe, DMT is Droplet Measurement Technologies, AIMMS is Air Data Probe, and CCN is Cloud Condensation Nuclei.

the month of May, the pre-monsoon period, to characterize the aerosol distribution close to the foothills. The flights were conducted basically to understand the aerosol-cloud interactions and also to measure the background aerosol concentrations. Most of the flight observations were done by performing cloud penetrations at several vertical levels. However, the type of analysis presented in this study requires near horizontal flights and such flights were rare. Two near-horizontal flight records were available on 27 May 2009, with flight path at an average height of 6.6 km, which were aimed at studying the aerosol distribution over the slopes. The horizontal extent of the flight path is 300 km and of 45 min duration.

[11] The CAIPEEX observations used for the study consist of vertical velocity, temperature, humidity and aerosol concentration measured at 1 Hz resolution. The aircraft speed was approximately 100 ms^{-1}, thus the spatial resolution of data is approximately 100 m. Table 1 lists the aircraft instruments on board the CAIPEEX aircraft and their range and resolution used in the study. Details of the experiment and instruments used can be found in *Kulkarni et al.* [2012]. The Air Data Probe (AIMMS from Aventech Research Inc.) is used to measure velocities and relative humidity. The Passive Cavity Aerosol Spectrometer Probe (PCASP SPP 200 from Droplet Measurement Technologies Inc.) is used to measure aerosol size distribution. All observations are synchronized in the Particle Analysis and Display System (PADS) software and further quality checks and corrections were carried out. Cloud Droplet Probe (CDP) derived liquid water content (LWC) was calibrated against Hotwire LWC probe derived liquid water content. Cloud condensation nuclei (CCN) observations are taken at three (0.2%, 0.4%, 0.6%) supersaturations. CCN data was pressure corrected and those data with CCN instrument inlet pressure greater than atmospheric pressure are rejected. This also implies that, though some of the observations would have been taken at higher elevations along the horizontal flight track, those CCN data are not used for the analysis. MODIS Level 2 observations of Aerosol Optical Depth at 550 nm and CALIPSO total attenuated backscatter intensity are used in the analysis. The aircraft observations were coordinated to have near simultaneous observations with MODIS and CALIPSO.

[12] With the objective to investigate the interaction between different scales, the spectral and cospectral characterization of the data and separation of variance at different scales of motion are performed using wavelet analysis. Wavelet analysis [*Daubechies*, 1991; *Farge*, 1992; *Meyers et al.*, 1993] is widely used for spatiotemporal analysis of atmospheric data [*Galmarini and Attié*, 2000; *Attié and Durand*, 2003; *Cornish et al.*, 2006; *Thomas and Foken*, 2007]. A continuous wavelet transform using Morlet wavelet function [*Grossmann and Morlet*, 1984], which is a plane wave modulated by a Gaussian, is used in the study. The wavelet analysis is carried out on time series corresponding to approximately 300 km flight distance sampled at 1 Hz, i.e., at 100 m spatial resolution. Each time series is normalized by standard deviation of respective parameter before subjecting it to wavelet analysis. The wavelet cross-spectrum [*Terradellas et al.*, 2001; *Cuxart et al.*, 2000] between the time series of vertical velocity and quantity x [temperature (T) or aerosol concentration (a)] is given by,

$$CW_n^{w,x}(s) = s^{-2} W_n^w(s) W_n^{x*}(s). \quad (1)$$

where CW_n is the wavelet cross spectrum, s is scale w is vertical velocity, '*' indicates the complex conjugate.

[13] Numerical simulations using Advanced Research Weather Research and Forecasting (ARW V3.3, http://www.wrf-model.org/) model are used to investigate the flow structures and trajectories close to the Himalayan foothills and CCN transport in the region. There are 2 nested domains at 9 and 1.8 km resolution. The outer domain (19.2°N–36.5°N, 65.7°E–91.8°E) is mainly used to generate the boundary conditions for the inner domain and to investigate some of the synoptic scale features not covered in the inner domain. The inner domain (28.5°N–34.6°N, 74.4°E–82.1°E) has 375 × 395 grid points with the aircraft flight track at the center of the domain. The parameterizations used are Yonsei University (YSU) Planetary boundary layer (PBL) scheme [*Hong et al.*, 2006] coupled with the Monin Obukhov (MO) similarity for the surface layer, Noah land surface scheme [*Chen and Dudhia*, 2001] Kain Fritsch scheme in the outer domain and cloud permitting in the inner domain, and WRF double moment 6-class (WDM6) microphysics scheme. WDM6 scheme enables the use of prescribed CCN concentration as initial conditions based on observations. CCN observations at 0.2% SS was too low for 27th May and was not used for the CCN spectra estimate, instead 28th May below cloud observations are used. The CCN spectra estimated for the flight on 28th May has a 'k' coefficient of 0.61 and the estimated CCN at 1% supersaturation is 15,263 cm^{-3} (from Prabha *et al.* under revision in JGR). A modified version of WDM scheme [*Lim and Hong*, 2010] with a correction to boundary condition is used in this study. The initialization of the model is done with the help of final analysis (FNL) data available from National Center for Atmospheric Research. The model initialization was done at 18 UTC on 25 May 2009 and simulations were done until 00 UTC on 28 May 2009. Boundary of the outer domain was updated at 6 hourly intervals with the

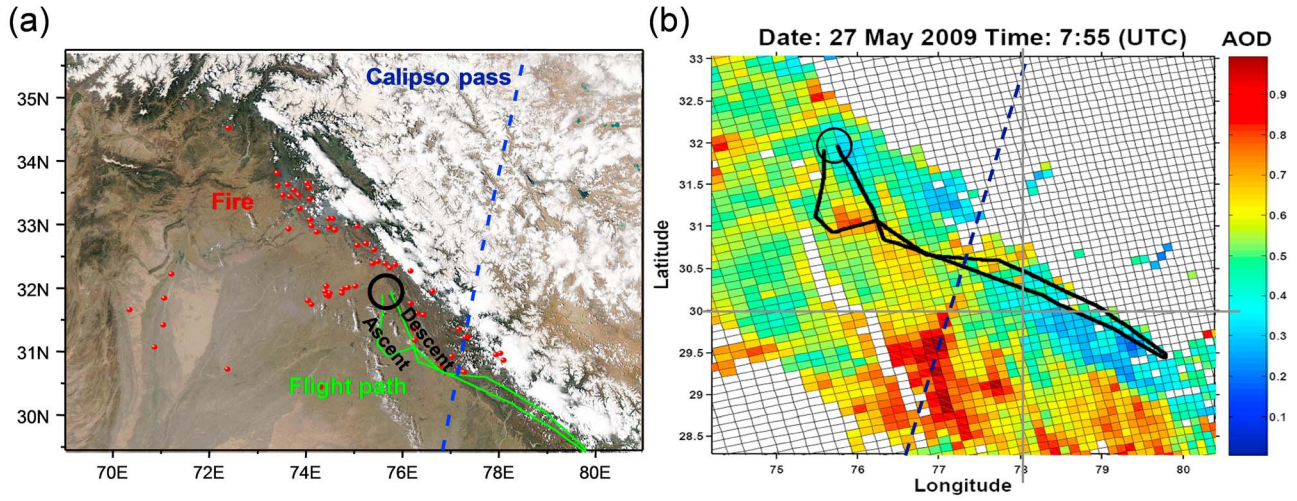

Figure 1. (a) Fire events (in red) along north Himalayan region during CAIPEEX observations on 27th May. (b) Aircraft flight path is shown in black and Calipso pass is shown in blue dashed line. MODIS Aqua observations of aerosol optical depth in relation to the aircraft flight path and Calipso track.

same FNL data set. The model runs were carried out in two way interactive mode.

3. Results

3.1. General Characteristics of the Case

[14] Pre-monsoon conditions existed on the day of the observation (27 May 2009) with dry and polluted conditions inhibiting cloud development. The study region was under the influence of northwesterly and westerly winds associated with a high pressure area located over the Middle East. The air mass trajectories in the lower and middle atmosphere originated from the continental regions of Middle Eastern landmass and the upper level trajectories showed subsidence over the study region. MODIS true color image showed hazy conditions with very little cloud development in the Ganges valley or over the foothills. MODIS observations showed a significant number of fire events in the foothill region, which are mostly related to agricultural burning events. The 48 hour fire records from MODIS are shown in Figure 1a along with the CAIPEEX flight path and CALIPSO pass. It is to be noted that the aircraft flight path intersected previous day's CALIPSO night pass (20:58:43 to 21:00:13 UTC) on 26 May (shown in Figure 1a). Analysis of MODIS, CALIPSO, CAIPEEX aircraft data and thermodynamics from radiosonde ascents are discussed in the subsequent subsections.

3.1.1. Qualitative Comparison of MODIS and Aircraft Observations of Aerosol

[15] The MODIS Level II observations of AOD presented in Figure 1b indicate the presence of high aerosol optical depth exceeding 0.9 along the CALIPSO path. Co-located MODIS observations along the aircraft flight path are used in Figures 2a and 2b to analyze the horizontal variations. It should be noted that MODIS AOD represents the total integrated aerosol attenuation in the column, while aircraft observations indicate the number of aerosol particles per unit volume in the in situ air samples. Daily average NO_2 (in units of molecules m^{-2} from OMI satellite) over these longitudes is also shown in the figure, indicating that fire emissions were present. There is considerable variation of AOD along the flight track. Although there is high AOD at several locations, aircraft observations show very low concentration of aerosol. High AOD is likely associated with attenuation due to aerosol present below the aircraft observation level. The horizontal aircraft flight observations were conducted over a haze layer.

[16] Here we would like to investigate whether there are instances where aerosols are transported above the haze layer in the absence of clouds. For the majority of the flight track, the aerosol concentration is very low (≈50 cm^{-3}) and much less variable, except for a few instances. Some of the occasional increase in the aerosol concentrations in Figure 2a are associated with cloud penetrations (marked with boxes, this aerosol data inside cloud is not used in the analysis). However, in Figure 2b, there are a few aerosol peaks (marked with boxes) that are not associated with presence of clouds. There are some collocated peaks in aerosol concentration and high MODIS AODs. At longitudes between 78.0 and 78.5°E over the slopes, peaks in aerosol concentration exceeds 1000 cm^{-3} and an increase in AOD is also noted. (Figures 2b and 2c). There were no cloud penetrations during this time and vertical velocity oscillated around 2 ms^{-1}. It may also be noted that the temperature increased at this period by 1°C. The CALIPSO aerosol subtypes did indicate the transport of smoke to higher altitudes and it is very likely that the heat transport is also taking place in these convective plumes. The question is; what is the cause of this vertical motion and is it purely driven by topography? We will investigate this aspect with numerical modeling which does not incorporate any fire emissions.

[17] The analysis of aircraft cloud penetrations (8:07:50 UTC to 8:09:49 UTC corresponding to a horizontal distance of 19 km) shown between 77.5 and 78°E in Figure 2a is presented in Figure 2d. This cloud developed on the slopes in the haze layer and had high concentrations (≈400 00 L^{-1}) of ice crystals at −17°C. Cloud top was approximately 6.8 km and the cloud penetration was 150 m below the cloud top. An examination of the vertical velocity associated with this cloud penetration illustrated a coherent upward (>4 ms^{-1}) and downward directed motion (Figure 2d). The increase in the vertical velocity

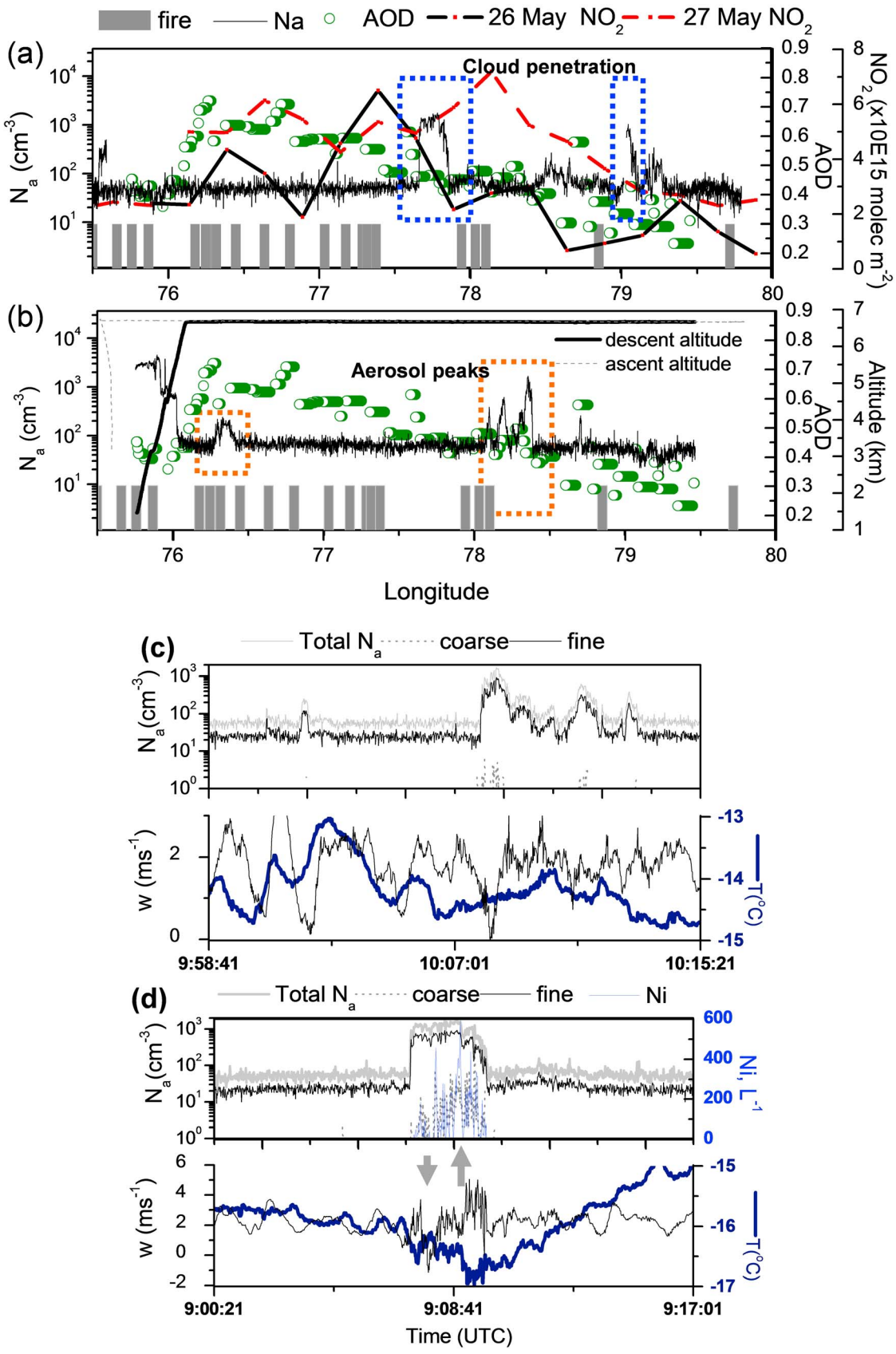
fire
Na
AOD
26 May NO2
27 May NO2
(a)
Cloud penetration
Na (cm-3)
AOD
NO2 (x10E15 molec m-2)
(b)
descent altitude
ascent altitude
Aerosol peaks
Altitude (km)
Longitude
(c)
Total Na
coarse
fine
w (ms-1)
T(°C)
9:58:41
10:07:01
10:15:21
(d)
Ni
Ni, L-1
Time (UTC)
9:00:21
9:08:41
9:17:01

Figure 2

associated with the cloud induced oscillations in the vicinity. Here the question arises; whether there is some indication of lifting of pollution to higher levels due to the convection near clouds? Aerosol concentration increased on both sides of the cloud penetration marginally (100–150 cm^{-3}, mainly the fine mode). Associated with this event, CCN concentration was found to increase in the neighboring locations, however at this altitude, due to strict pressure corrections applied for CCN data, this increase could not be justified. So this leads to the second question of whether the convection and clouds along the slopes of Ganges valley increases the aerosol transport to the Tibetan plateau.

3.1.2. CALIPSO and Aircraft Observations: Vertical Profiles

[18] CALIPSO total-attenuated backscatter observations over the slopes and Ganges valley have indicated presence of high amount of aerosol in the elevated layer (Figure 3a). Such elevated pollution layers have been observed in past observational campaigns from ground based observations [*Ramana et al.*, 2004; *Raj et al.*, 2008; *Satheesh et al.*, 2008; *Srivastava et al.*, 2011] and also during CAIPEEX campaign over several locations in India [*Kulkarni et al.*, 2012]. *Srivastava et al.* [2011] reported Lidar observations on the slopes with dust layer peaking at 1.5 km and extending up to 3 km for both pre dust and dust days. Their back trajectory analysis clearly indicated a decent of trajectories on several days before the ascent to 1.5 km. This is a clear indication that even the dust transport from Thar Desert is not a pure horizontal advection due to strong winds, rather is influenced by strong vertical motion as well. The concentrations of aerosol measured at elevated layer in the Gangetic area during CAIPEEX are much higher (2 orders of magnitude higher) than that over the low latitude locations [*Kulkarni et al.*, 2012]. This difference is noticed at elevated layers as well. It may be noticed that the regions close to the foothills show less attenuated backscatter, indicating less aerosol concentrations close to the slopes. However, at locations away from the slopes, there are indications of high aerosol concentrations, especially at some elevated layers. The CALIPSO pass indicated a well mixed layer close to the foothills and an elevated pollution layer (EPL), few hundred kilometers (>200 km) away from the foothills area. This EPL region has lower levels of pollution in the lower part of the boundary layer and higher pollution layers aloft (4–6 km layer).

[19] The aerosol extinction vertical profiles are presented in Figure 3b for 26 May and also for monthly average of May 2009 to illustrate the difference over different distances from the slope. For this purpose, the aerosol attenuation for four selected latitudinal belts is considered (A: 23–25°N; B: 25–27°N; C: 27–29°N; and D: 29–30°N) along 77.5°E. The elevated layer with high attenuation and high pollution away from the slopes is also noted for the May 2009 monthly average presented for same latitude sectors along 77.5 E. This behavior is not a characteristic of the location in the current study alone. CALIPSO transects at other latitudinal sectors also show similar characteristics on several days. The elevated pollution layer away from the slopes and a cleaner well mixed layer near the slopes are evident. High pollution away from the slopes is especially noted. Aerosol subtype characterization plot for 26th May (Figure 3c) showed clear indications of smoke plumes along the slopes (marked A) reaching 3.5 km above msl. The polluted dust reached 4–5 km higher over the Plains (marked B) and extends to further southern latitudes (marked C) during the Calipso pass of 26 May night. The daytime Calipso pass on 27 May at 7:45 UTC at a location 300 km east of the area of our interest showed presence of smoke reaching to a height of 3.5 km in the Foothills area (marked D) and presence of polluted dust reaching to 4–6 km above msl on the slopes. This is further indication that daytime smoke rising and dust getting polluted with the smoke rise over the slopes.

[20] The aircraft observations of aerosol concentration are presented in Figure 3d. The aircraft observations started from Pathankot (32°17′N, 75°39′E) air strip in the valley and proceeded toward the summit of the mountain at a height of 6.6 km above the surface. Vertical variation of aerosol fine (0.1–0.3 μm) and coarse (0.5–3.0 μm) mode during the ascent and descent, CCN concentration at 0.4% and 0.6% SS during the ascent are presented in Figure 3d. The low-level aerosol concentration from aircraft observations (Figure 3d) showed a remarkable resemblance to the CALIPSO attenuation profiles (Figure 3b on 26th May) with a 4 km deep polluted layer. Peak aerosol concentrations are noted in the 3–4 km layer above the surface, with lower and well mixed concentrations in the layers below. The boundary layer was approximately 2.7–3 km deep with a very weak entrainment layer inversion (which is more clearly visible in the radiosonde data presented in Figure 4b and discussion on thermodynamics). The research aircraft ascent was approximately 50 km away from its descent at certain locations. The ascent lobe of the flight (Figure 3d, away from the slopes) showed higher concentrations of aerosol compared to the descent lobe (close to the slopes) in the 3–4 km layer. This information, along with the CALIPSO observations (Figure 3b) on several other days indicates that aerosol concentrations were low, close to the slopes (<50 km) compared to those farther away from the slopes. Aerosol concentrations are less than 1000 cm^{-3} in the 4–6.5 km layer. The horizontal flight segment (indicated with a box in Figure 3d) of the aircraft was at 6.6 km, which showed aerosol concentrations up to 2000 cm^{-3}. The 6.6 km level horizontal flight path was over the northeastern sector of the local airport toward Nepal, along the slopes.

[21] Figure 3d also gives vertical profiles of cloud condensation nuclei observed at 0.4% SS (CCN observations at 0.2% were also carried out, however are not used here). The CCN concentrations are very close to the aerosol concentrations, indicative of the dominating fine mode particle concentration at all levels. The fine (0.1–0.3 μm) and coarse

Figure 2. Comparison of fire events, aircraft observations of aerosol concentration (Na) from flight records and aerosol optical depth (AOD) from MODIS along longitudes: (a) during aircraft ascent and (b) during the descent. OMI NO_2 for 26 and 27 May is also presented in Figure 2a. Simultaneous observations of aerosol (Na), fine and coarse mode aerosol, temperature (T) and vertical velocity (w), showing updrafts and downdrafts at constant altitude of 6.68 km associated with (c) the aerosol peaks and (d) cloud penetration 150 m below the glaciating cloud top. Ice concentration (Ni) is also shown in Figure 2d.

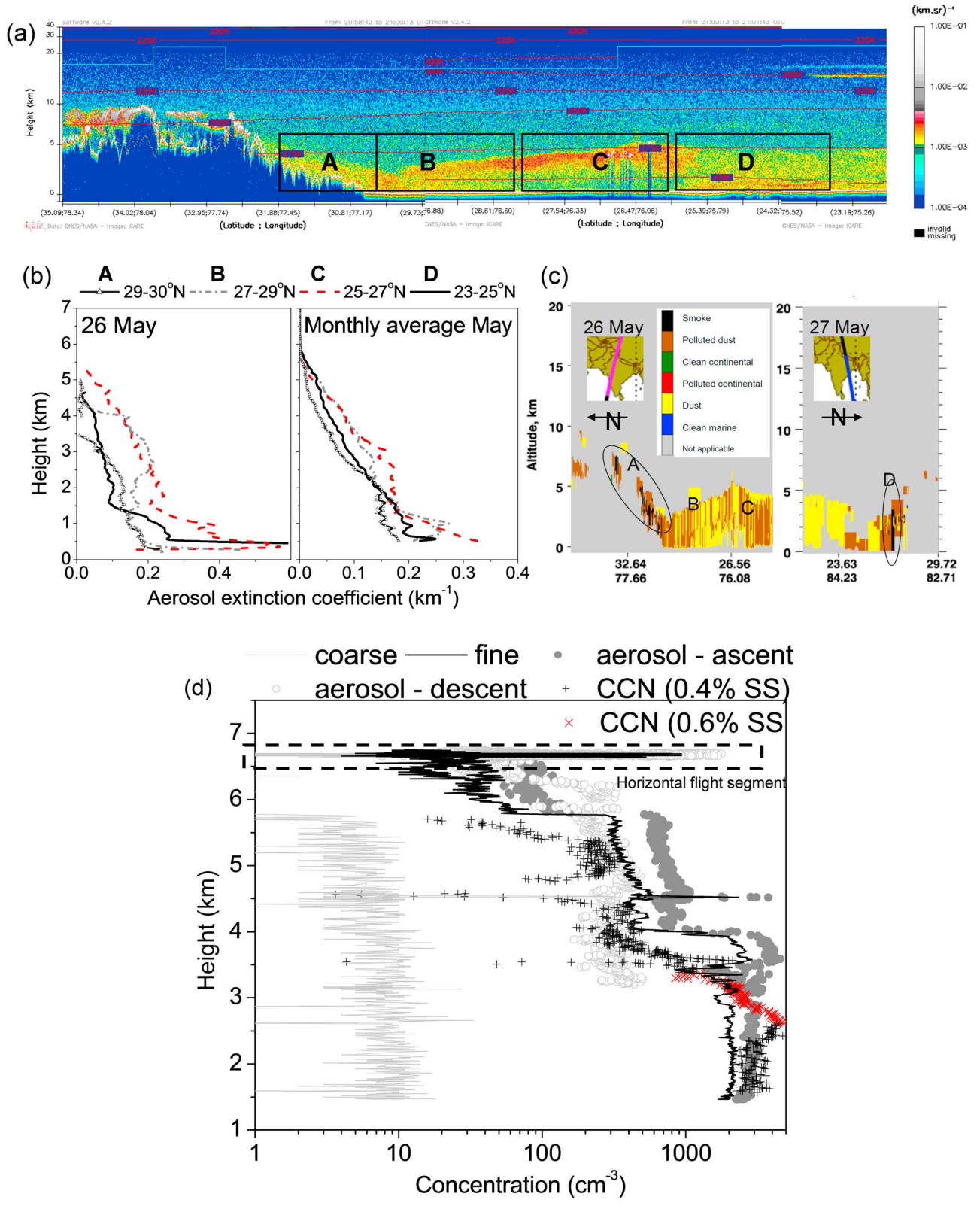

Figure 3. (a) Calipso total attenuated backscatter at 2000 UTC (0100 IST) on 26 May 2009. (b) Vertical profiles of aerosol extinction from Calipso observations on 26th May for monthly averaged values for May 2009. (c) The aerosol subtypes for 26 May and for 27 May. (d) Vertical profiles of aerosol (coarse and fine), and CCN concentration (at 0.4% and 0.6% SS), and total aerosol concentrations from CAIPEEX research aircraft observations during the ascent and descent.

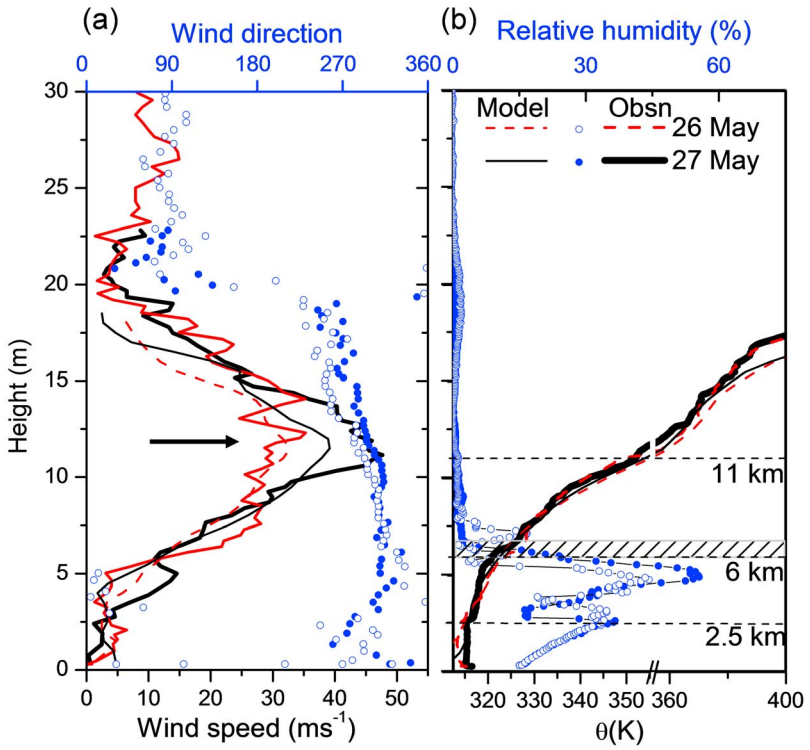

Figure 4. Radiosonde (a) wind speed and (b) potential temperature observations for 26th May (thin line) and 27 May (thick line). A strong westerly mid tropospheric jet at 10.5 km level is noted. Extra thin lines are model results.

(0.5–3.0 μm) mode concentrations derived from aircraft aerosol size distribution are also presented. A higher elevation (1939 m) AERONET station Nainital (29.36°N, 79.46°E) close to the foothills reported an increase in the daily average fine mode AOD that varied as 0.15, 0.19 and 0.28 on 26, 27 and 28 May respectively. Coarse mode daily average AODs are 0.16, 0.12 and 0.26 respectively on 26, 27 and 28 May.

3.1.3. Thermodynamics of the Case

[22] The thermodynamic conditions were not favorable for cloud development. Estimated convective available potential energy (CAPE) from radiosonde observation was 870 Jkg^{-1}, precipitable water was 2 cm, and temperature at lifting condensation level (LCL) at height 636 hPa was 3°C. Radiosonde observations (Figure 4) from Pathankot (32°17′N, 75°39′E) showed a strong westerly jet at 11 km level with maximum speed of 34 ms^{-1} on 26th May and 45 ms^{-1} on 27th May at 1100 IST. Model simulated wind speed at this location is also presented in Figure 4a. Wind direction is much variable below 5 km (Figure 4a). These changes in wind direction are associated with the channeling effect in the valley (noted with northerly wind component) as mean flow gets adjusted to the surrounding terrain in the Pathankot area. The potential temperature from radiosonde data also shows that boundary layer (BL) height was 2.7 km (Figure 4b) with a weak inversion layer. The entrainment layer was shallow (<200 m) and not noticeable when compared to other regions such as the Saharan Boundary layer [*Huang et al.*, 2010]. Such dry adiabatic boundary layers can reach up to 6 km as in the case of Saharan boundary layer [*Gamo*, 1996] with a combination of a convective boundary layer (CBL) and a residual boundary layer (RL) above the CBL. The possible role of dry thermal convection in transporting heat from the surface to the upper troposphere was indicated in the early studies over the Tibetan Plateau by *Luo and Yanai* [1984]. The residual layer constitutes previous day's characteristics such as the pollution/moisture transport and would still be convectively active. This condition is also noted in the radiosonde observations with a convective layer above 2.7 km, reaching to 6 km. Stronger inversions are seen above 6 km. On 27 May there is a clear indication of the multiple convective layers, while on 26 May the elevated layer (2.5–6 km) is weakly stable. The variation of relative humidity (Figure 4b) indicates a layering structure associated with horizontal advection rather than a moisture source from the boundary layer, which was dry (RH < 20%). The Thar desert is in the neighborhood of the observational area and dust emission from this area was evident on 17, 21 and 24 May, as indicated by the Ozone Monitoring Instrument (OMI) satellite data, showing AOD > 0.8 (OMI AOD data is not shown). In addition, the fire emissions from the surface seem to have lifted to the residual layer. This is evident from higher pollution episodes along the flight path as illustrated from the MODIS and aircraft observations as discussed earlier.

3.2. Analysis of Scales of Interaction

[23] To investigate the dynamical interaction at a specific level, we have considered a near-horizontal part of the flight data from a two-hour transects (Figure 5). From this transect, two periods of 45 min duration each are considered; (A) a case with a small portion of cloud with 14 s cloud pass corresponding to approximately 1.5 km, liquid water content of 0.03–0.27 g^{-3}, cloud droplet number concentration

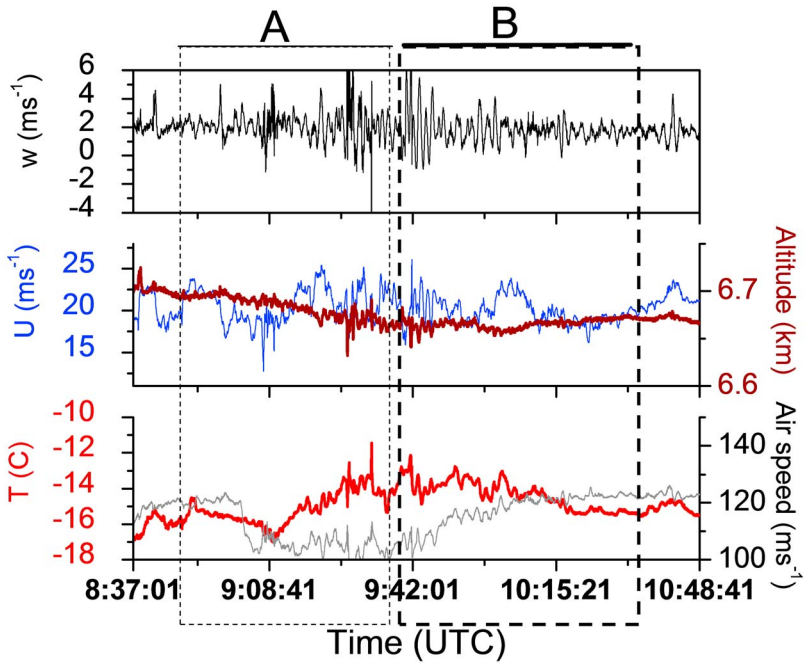

Figure 5. Flight observations of vertical velocity, horizontal wind speed and air temperature. The segments of flight (A and B) indicated for cloudy (segment A) and cloud free (segment B) conditions used in the wavelet analysis and for the spectrum. Right y axis is altitude.

(CDNC) of 71–333 cm^{-3} and effective radius of 5.1–6.8 μm) and (B) without clouds (CDNC < 20 cm^{-3}). These 2 cases are subjected to wavelet analysis (shown by A and B in Figure 5). The analysis is grouped into 'with cloud' (marked A) and 'without cloud' (marked B). There is considerable variation in the vertical velocity (up to 5 ms^{-1}) in the regions of high concentrations of aerosol (already illustrated in Figure 2c), which are identified to be on the slopes and were closely associated with gravity waves. In addition to these data sets, the flight data from 26 May away from the slopes is also used in the spectral analysis.

[24] Spectral energy calculated for all three velocity components are presented in Figure 6 (top panel). The 45 min flight segments considered here cover a distance of 300 km and flight records data at 100 m resolution. Spectra follows −5/3 slope (indicated in the figure) for the mesoscale range [*Lilly*, 1983], however regions with buoyancy ranges (slope ≈−3) are also noticed. Energy gap is not visible due to dominating large-scale motion. The inertial sub range corresponding to small-scale turbulence is not covered by data. All three velocity spectra merge at wavelengths 800 m to 11 km in the absence of clouds, indicating spectral isotropy. The spectrum is non-isotropic when clouds are present due to several high frequency energy contributions, which are possibly due to gravity waves generated by convection and increased turbulence with the cloud. The gravity waves also seem to propagate from the region of their origin and can be present in pockets away from the cloudy region (Figure 2d, showing the vertical velocity and temperature variation around the cloud illustrate this aspect with several long period oscillatory features, also note that they are 90° out of phase). These types of events cause several low frequency contributions to energy, which are also noted to be more in the cloudy case. Gravity waves are omnipresent as can be noted at the high wavelength part of the spectra. The spectral peak at 10–11.5 km wavelength range evident in both the w spectra indicates an energy source (Figure 6a), and it matches with the height of the jet discussed earlier (Figure 4a).

[25] In the presence of cloud, energy increases in the higher wavelength, however the peak is retained at the same wavelength. Does this mean that vertical motions at this level are rather constrained by the jet? To address this question, we investigated vertical velocity spectrum from a flight approximately 100 km away from the slopes as well (for 26 May, also shown in the figure). It may be noted that the peak noticed at 10–11 km is not present in such a case, however energy corresponding to low-frequency variations have increased. Direct numerical simulation (DNS) result of a far jet (jet is located far from the shear layer) presented by *Pham and Sarkar* [2010] may be relevant here. In stably stratified flows with shear, the internal waves in the presence of a far jet did not penetrate the jet layer, however were trapped inside the region between the shear layer and the jet [*Pham and Sarkar*, 2010]. They have illustrated a peak horizontal wavelength, which is equal to the wavelength of the most unstable mode. In our case, this wavelength may correspond to the terrain height encountered, which is approximately 10–12 km.

[26] To investigate the vertical exchange, the momentum, heat and aerosol are analyzed in Figures 6d, 6e, and 6f. The following points could be noted: in the absence of clouds, the dominant peak in the heat flux is upward directed at 11.5 km wavelength, indicating that there is transfer of heat to higher levels at this wavelength. The momentum and aerosol flux (not shown) peaks are also centered on this wavelength. This gives a clear indication that the convective plumes associated with the fire emissions (Figure 2c; we noted these plumes in the time series of vertical velocity and temperature) are able

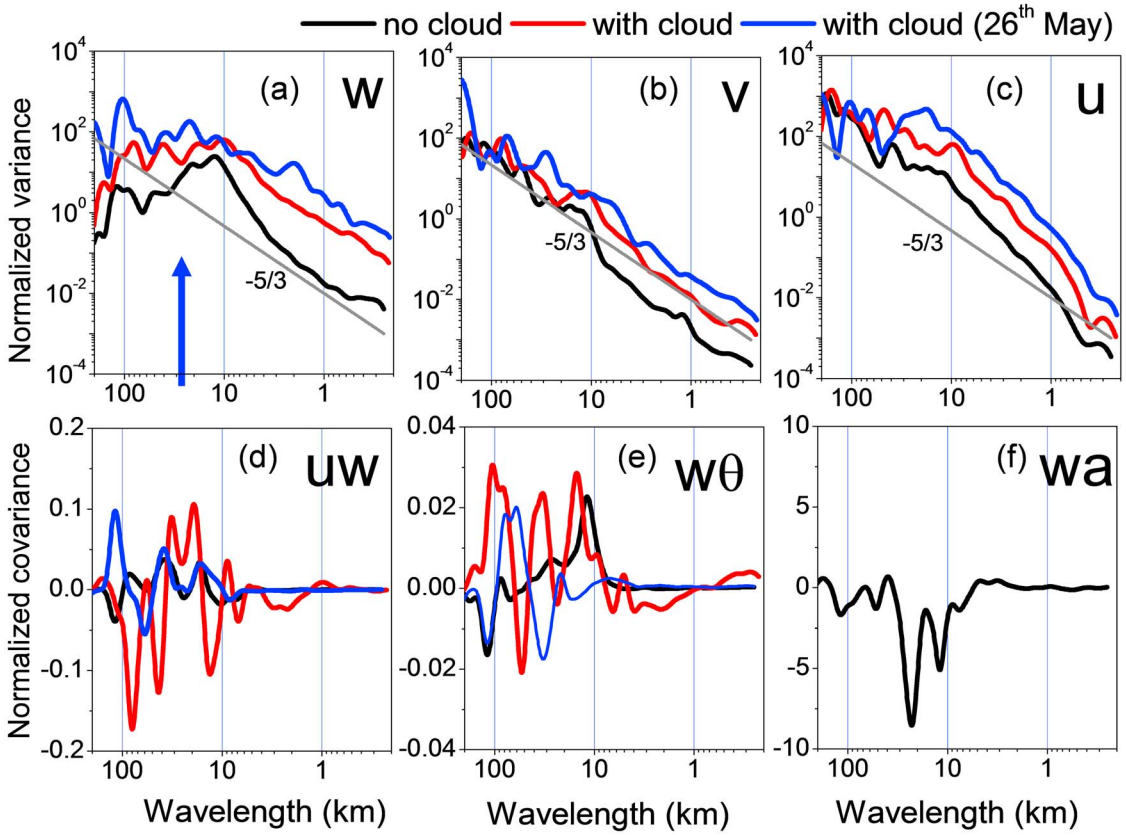

Figure 6. Energy spectra of velocities with and without cloud and from another horizontal flight data 50 km away from the slopes: (a) variance spectra of vertical velocity, (b) u component of velocity and (c) v component of velocity, and the cospectrum for (d) momentum, (e) heat and (f) aerosol vertical flux. Note that for aerosol vertical flux, only cloud free data are used.

to make a difference in the energy fluxes. In the presence of cloud, there is increase in the fluxes at all wavelengths. The peak in heat flux is still present, but there is another peak at higher wavelength (∼15 km). The reason for such behavior may be attributed to the presence of low frequency gravity waves generated due to convection and are able to propagate horizontally in a sheared and stratified environment.

[27] Since the wavelet decomposition could be used to separate variances at different scales, we use wavelet analysis to look at the variances of temperature and vertical velocity associated with <3 km, 3–11 km, and 11–100 km wavelengths (this scale separation is based on the characteristic scale of 11 km seen in the vertical velocity spectra, in the traditional context termed as local scale, and meso gamma and beta scale with an overlap – note that there is a part of the turbulence scale associated with this local scale - the spectra do not cover the inertial subrange and could not be treated as turbulence). Figures 7a and 7b show decomposed temperature and vertical velocity variances in the absence of cloud. 11–100 km scale variance is the dominant one. There is a periodic behavior in the 3–11 km scales (Figure 7b). At wavelengths <3 km, fluctuations appear random, however, there are instances when all three scale variances are well correlated in their variations with space, which are corresponding to the cloud passes in the cloudy case and associated with strong updrafts with high pollution in the cloud free case. In the cloud free case, the 3 km scale variance is much smaller than the meso scales. However, with temperature variance (Figure 7c), the mesoscale, and local scale are well correlated in the cloudy case and have approximately the same variance during the cloud pass or when vertical velocity is high. Analysis of the cloudy conditions show that (Figures 7c and 7d) the energy at smaller scale increases and all three scales have nearly equal contribution to variance when clouds or pollution are present.

3.3. Inferences From Numerical Model Simulations

3.3.1. Surface Layer and Boundary Layer Features

[28] Model simulations are conducted to investigate spatial distribution of the flow fields and CCN close to the slopes and how the vertical velocity spectra close to the foothills are represented in the model. Initially we investigate the model simulation over the region in regard to reproducing the surface layer and boundary layer characteristics. Surface observations for model verification during the study period are limited to the India Meteorological Department (IMD) observations from two locations, one over the slopes (Mashobra at 31.1°N, 77.2°E, 2270 m above msl; called 'slope station') and other in the desert area (Jhunjunu 28.3°N, 75.6°E, 301 m above msl; called 'Plains station'). These observations are used (Figure 8a) only for qualitative comparisons to investigate whether the model is able to reproduce the diurnal features over the Plains station and over the slope station. The 2 m level air temperature

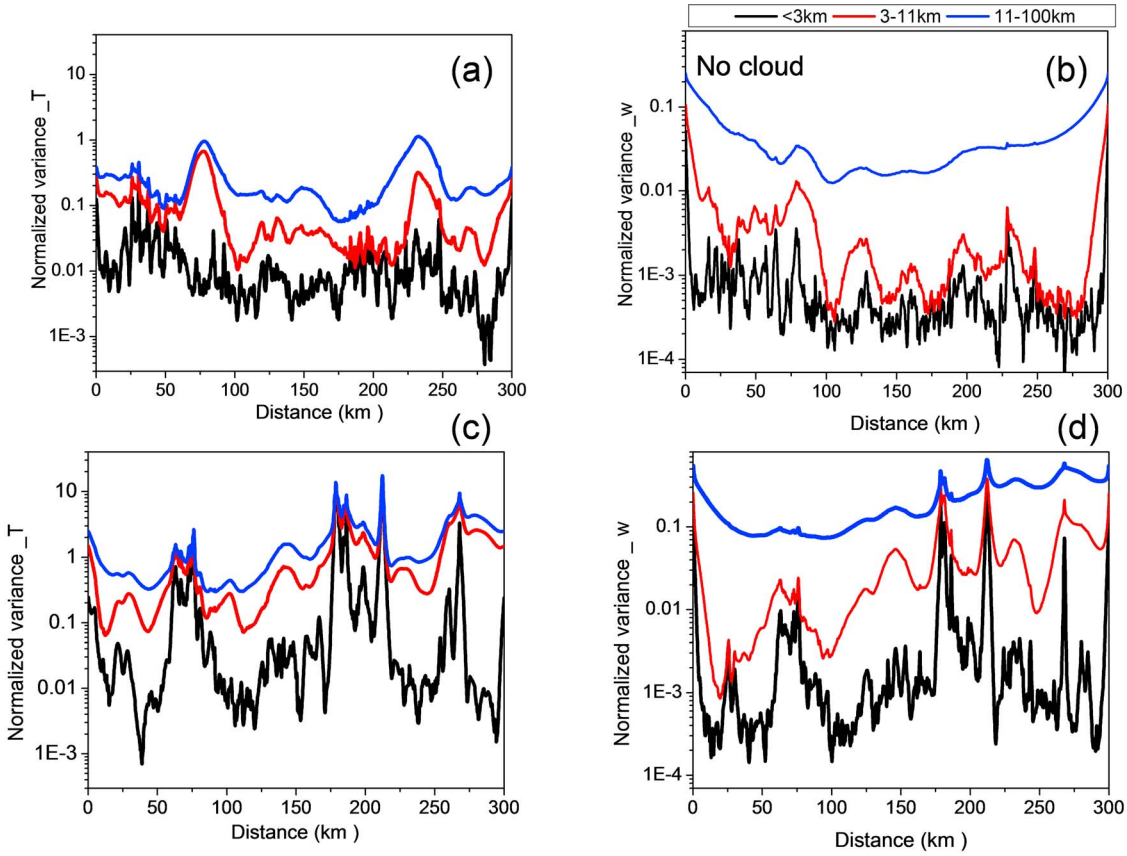

Figure 7. Scale separated variance associated with wavelengths of <3 km, 3–11 km and 11–100 km: normalized variances of (a) temperature without cloud, (b) vertical velocity without cloud, (c) temperature and (d) vertical velocity with cloud.

(Figure 8a) showed diurnal evolution as in the observation and the horizontal temperature difference is also reproduced well in the model. Surface winds were stronger (3–7 ms^{-1}) over the Plains station. There is a difference of incoming radiation of 50 Wm^{-2} between the slope and Plains stations, which caused a difference of 35 Wm^{-2} in the sensible heat flux. Early heating (a phase difference of one hour is noted) over the slope station caused this difference.

[29] Latent heat flux showed a diurnal variation and reached diurnal maximum of 200 Wm^{-2} near the slope station however over the Plains it was less than 5 Wm^{-2}. This difference is attributed to the soil moisture (14% over the slopes compared to 7% over the Plains station) and thus potential evaporation differences as there was no rainfall simulated at both locations. The latent heat flux (LE) was maximum at latitude of 33.5°N and it decreased northward and southward from that point. The LE remained positive (50–150 Wm^{-2}) during the night over the latitudes 33–34°N. Some of the observations over the Tibetan Plateau by *Ma et al.* [2005] showed such nocturnal LE. Nocturnal surface winds also increased over this region and the slope and valley winds generated in the tributary valleys are noted. The 10 m level wind speed increased to 14 ms^{-1} over the valley points during the night and such accelerations have been noted in observational studies [*Shrestha and Barros*, 2010]. Ground heat flux showed a difference of 80 Wm^{-2} between the Plain and the slope stations. The long wave (LW) radiative flux over the plains was 360 Wm^{-2} compared to 280 Wm^{-2} over the slopes. The energy partitioning over the slopes and the Plains need to be understood from the observations, which is not available during this study. The PBL height (Figure 8b) over the slope is smaller than over the Plains and also peaked earlier in the day due to the phase lag of heating over the Plains station. Over the Plains station, deep PBL (up to 4 km) is noted in the late afternoon hours.

[30] The latitudinal variation of equivalent potential temperature (θ_E) (Figure 8c) and CCN distribution (Figure 8d) from the model is used to illustrate the variation of PBL depth and related transport of CCN. The perturbation potential temperature and water vapor mixing ratio is also presented in respective figures with contour lines. Different regions in the figures (Figures 8c and 8d) are marked to illustrate major features. There is deep BL as seen with high θ_E in the lower 4 km, 200 km away from the slopes (marked A in Figure 8c). There is also increase in θ_E near the slopes (marked B) indicating convection (as also noted in the change in perturbation potential temperature) and wavelike features further over the Tibetan plateau. Figure 8d illustrates high CCN concentrations at elevated layers with low (<6 gkg^{-1}) water vapor mixing ratio (marked C). On the slopes CCN concentration is low (marked D) and over the plateau small concentrations of CCN is noted.

[31] The CCN distribution showed similar features that were seen in the CALIPSO image (Figure 3a) with lower

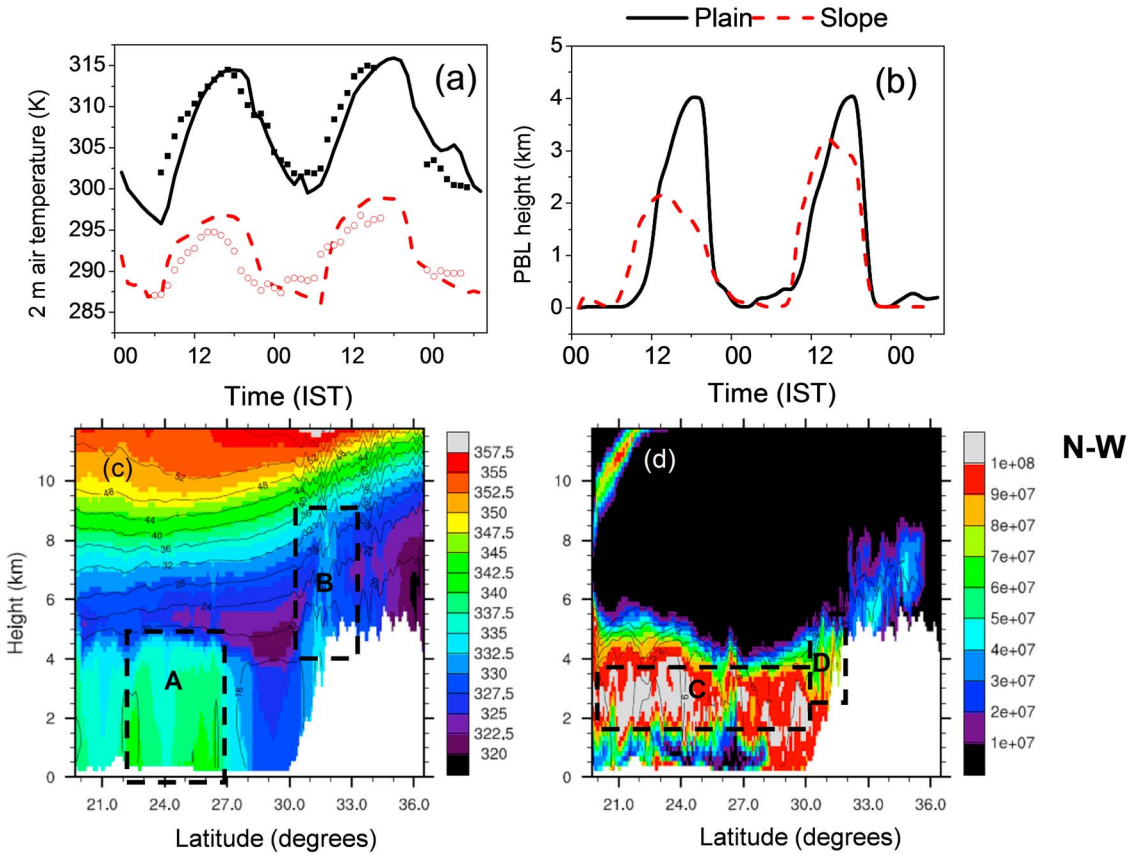

Figure 8. Variation of (a) air temperature, and (b) PBL height from the model in the Plain and over the slope. (c) Latitudinal variation of equivalent potential temperature (K) in color and temperature with contour lines, and (d) CCN concentration (in kg^{-1}) in color and water vapor (gkg^{-1}) in contour line. Deep and dry boundary layer convection in the plains (A), convection close to summit pertaining to 10 km (B), high CCN in the elevated layer (C) and low CCN along the slopes (D) are noted.

concentration of aerosol close to the slopes and higher aerosol concentrations in the adjacent valley boundary layer and at elevated layer. This feature is well marked in the north-south transect (Figure 8d). The convection is noticed in updrafts reaching 4 km height. Maximum CCN concentration is noticed 2–4 km height, in the upper layers of PBL. It may be noted that the radiosonde vertical profiles at 1100 IST indicated the presence of variable gradient layer with a 2.7 km BL and a convective residual layer above (Figure 4b). The entrainment layer inversion was very weak. Further convection during the day caused lifting of that inversion and the two convective layers merged to form a deeper boundary layer. The pollution already present in the residual layer could contribute to the increase in the aerosol concentration in that layer. Another possibility for the introduction of more aerosol into this layer is discussed below.

3.3.2. Dynamical Effects Near the Slopes

[32] The detailed features near the slopes is investigated with an east-west (E-W in Figure 9) and north-south (N-S in Figure 10) cross section along the point (32°N and 78°E, at 0800 UTC see Figure 1b for the transect in relation to the aircraft flight track). This point is chosen such that it makes adequate representation of the topographic barrier effect across the aircraft flight track. Figure 10a shows horizontal wind speed in color and resultant (u and v) wind vectors. Data is scaled to maximum wind speed in the vertical plane (which is presented as *x 38.73* at the top corner of the plot). The mid tropospheric jet is noticed at 10–11 km level with a maximum speed of 38.73 ms^{-1} in the E-W transect (Figure 9a) and 40.57 ms^{-1} in the N-S transect (Figure 10a). Boundary layer wind speed in the valley is below 3 ms^{-1}, whereas BL winds exceed 3 ms^{-1} over the slopes, where there is also strong vertical velocity. Figures 9b and 10b shows maximum vertical velocity of 3 ms^{-1} (shown on the top right corner of the figure and results are scaled to this maximum value). The trajectories (between along wind and vertical velocity components in the E-W cross section, between cross wind and vertical velocity in the N-S cross section) are shown with contours.

[33] There are a few interesting features to be noted in the N-S transect (Figure 10b), which are marked with boxes. The strong updraft at the summit is compensated by a downdraft over the region 200 km south of the summit. The trajectories have an elongated nature toward the valley (marked A) and also creates a wake like feature. Model results of vertical velocity support the evidence of strong updrafts along the slopes extending to 4 km and higher at the summit (marked B). These updrafts also cause a region of downdrafts on the plateau (marked C). Further north of these

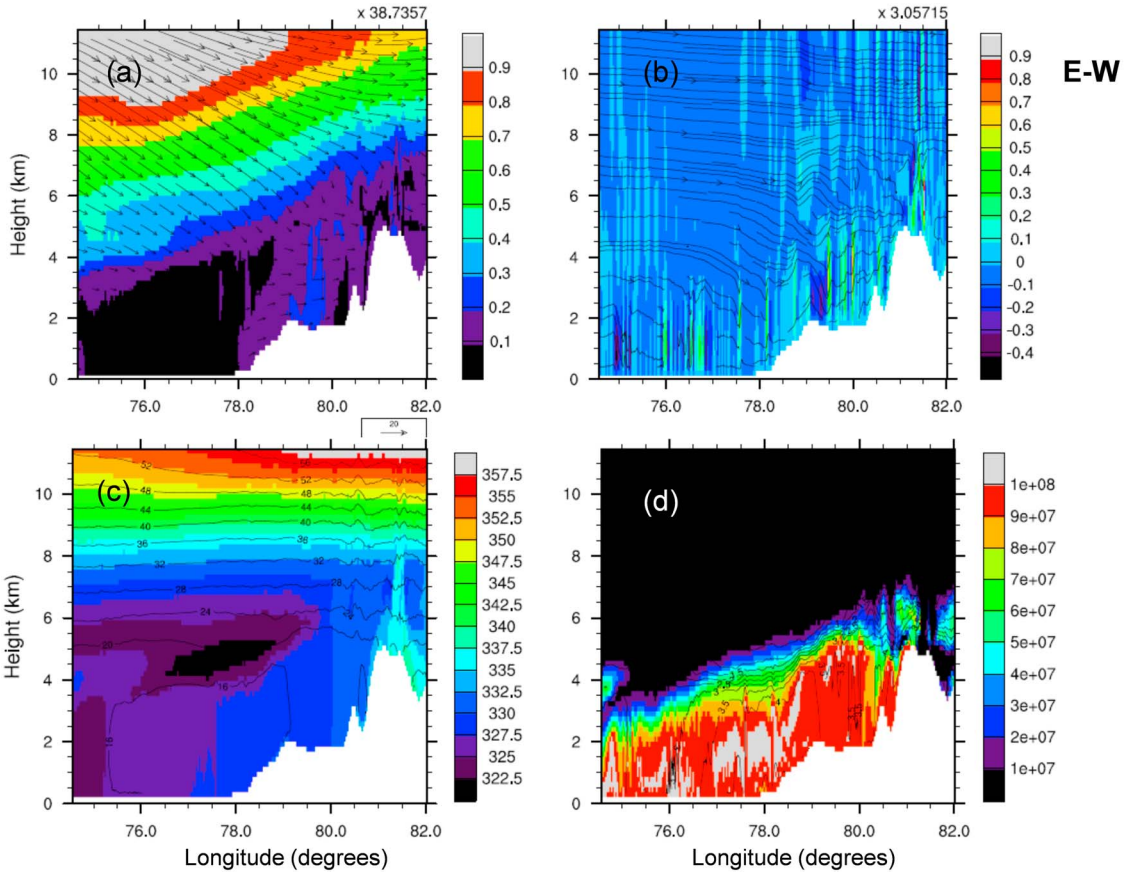

Figure 9. The east-west transect shown along 32°N for (a) horizontal wind speed and direction with vectors, and (b) vertical velocity (ms^{-1}) and streamlines of (cross wind; v and w). Vertical velocity and horizontal wind speed are scaled to their maximum values (shown on the top right corner of each plot). (c) Equivalent potential temperature (K) in color and perturbation potential temperature (K) in contour and (d) CCN concentration (in kg^{-1}) in color and mixing ratio in contour.

over the plateau, there are narrow updrafts and wide downdrafts, which do not penetrate to lower layers (<2 km).

[34] These updrafts are seen below the jet and are rather constrained by the jet. There is low-frequency gravity wave generation below the jet, but has smaller amplitude. It appears that the strong updrafts and wave generation is associated with lifting of air parcels above the summit. A strong updraft is observed very close to the slopes and is accompanied by wide downdraft area up to latitude of 28°N. These wide downdrafts are able to explain low wind velocity, low equivalent temperatures (Figure 10c) and low CCN concentrations (Figure 10d). South of 28°N, surface attached vertical motion reaching up to a height of 4 km is noticed in association with boundary layer convection.

[35] The temperature perturbation and the equivalent potential temperature (Figures 9c and 10c) give further indications of gravity waves propagating to higher levels, but are not amplified. The vertical propagation occurred in the regions where the jet was weak. Amplitude of these perturbations decreased over the plateau. A distribution of CCN concentration from the model and water vapor mixing ratio (in contour) is shown in Figures 9d and 10d. It may be noticed that water vapor transport does take place in strong updrafts, however does not reach to altitudes higher than 6 km.

[36] The horizontal distribution of model derived vertical velocity at 6.6 km during the aircraft observations is investigated in detail. Figure 11a gives vertical velocity from the 1.8 km resolution model run. Terrain height contours and aircraft flight track are also shown. The color map (black color for stronger updrafts and white for stronger downdrafts) is adjusted such that many small scale features can be identified. Maximum updraft is 10 ms^{-1} and downdraft is -4 ms^{-1}. Some of the interesting features noted are marked in the figure. Over the flight track, several gravity waves are noted (marked A). Gravity waves are also noted farther into the valley region (marked B) There are strong vertical velocities along the summit (marked C) and a region with downdrafts (marked D) at the plateau. Further north of this downdraft region, weak and wide downdrafts and strong and narrow updrafts are noticed (marked E). The topography over the plateau would have contributed to this unique feature. Our inferences show that the lifting of pollution to the Plateau takes place in several localized regions along the slope with strong updrafts unlike a likely large-scale lifting as proposed by *Gautam et al.* [2011].

[37] Another analysis was performed to investigate how the vertical velocity spectra from the observation and model are compared. Model data from the region of flight is used and the spectral analysis showed (Figure 11b) that model

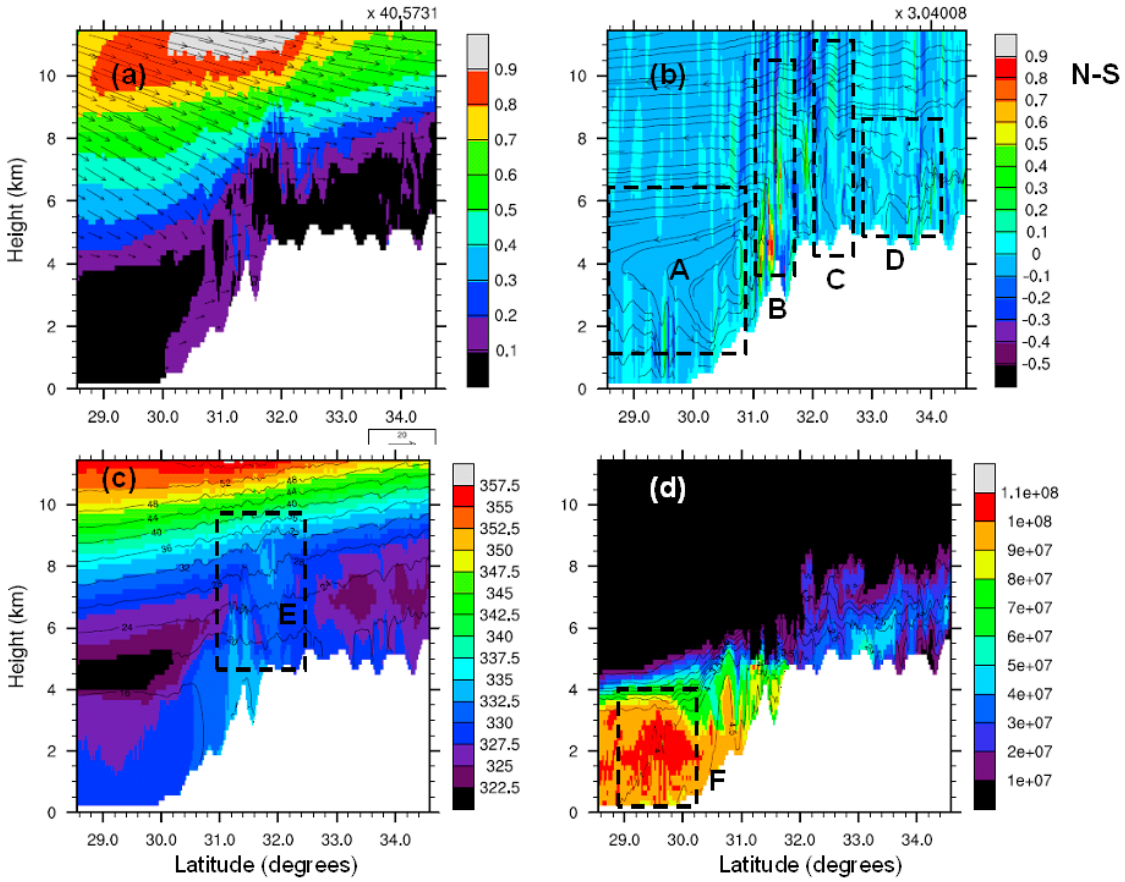

Figure 10. The north-south transect along 78°E for (a) horizontal wind speed and direction with vectors, and (b) vertical velocity (ms^{-1}) and streamlines of (cross wind; v and w). Vertical velocity is and horizontal wind speed are scaled to their maximum values (shown on the top right corner of each plot). (c) Equivalent potential temperature (K) in color and perturbation potential temperature (K) in contour and (d) CCN concentration (in kg^{-1}) in color and mixing ratio in contour.

spectral energy is underestimated when compared to that of observations. The error bars indicate the variation within the latitudes 28°N to 32°N. The observation showed more energy at all wavelengths larger than 20 km. However, there are indications in the model for the 10–12 km peak, as in observations. The underestimation of the spectra in the model could be related also to the effect of high resolution topography, which is smoothed in the model, even though 1 km resolution United States Geological Survey (USGS) data is used. Further study into the reasons for this underestimation will be conducted separately. Another important aspect is that spectral slope of −5/3 is reproduced by the model and the observations. Coarse resolution of the model (1.8 km) explains the lack of coverage at higher frequencies.

3.3.3. Characteristics of the Jet: Synoptic Scale Influence

[38] The spatial distribution of jet speed (Figure 12a), height (Figure 12b) and jet shear (ratio of jet speed and height of the jet) (Figure 12c) during the aircraft flight is presented. Speed and height of the jet decreased over the plateau and the jet shear is maximum along the slopes, which decreases toward north and south. Latitude versus time variation of the jet characteristics is also presented to investigate the synoptic scale influence. Speed and height of the jet are presented in Figures 12d and 12e respectively. The jet attained maximum speed during the aircraft observation (indicated with a box). The southward extent of the jet is also greater during this period. The jet height was low over the regions north of 30°N and the jet height increased in a narrow region close to the foothills (Figure 12e), where maximum strength was also noted (Figure 12d).

[39] Figure 12e shows the time-height variation of vertical component of vorticity (in color contour) and wind speed (in contour lines) at the slopes in the middle portion of the aircraft flight track. The interesting aspect is that there is production of vorticity below the jet which may assist the formation of scales of motion comparable to the jet scale, while restricting larger scale vertical motions. The shear sheltering theory proposed by *Hunt and Durbin* [1999] explains a mechanism by which increased shear may also result into reduction of turbulence due to increased vorticity below the sheared layer (whereas in typical conditions increase in shear leads to more turbulence). This effect play a role in the constraining of eddies in the boundary layer jets [*Smedman et al.*, 2004; *Prabha et al.*, 2008] and such effects in the vicinity of large scale jets needs further investigation. DNS study of far jet in stratified sheared case of *Pham and*

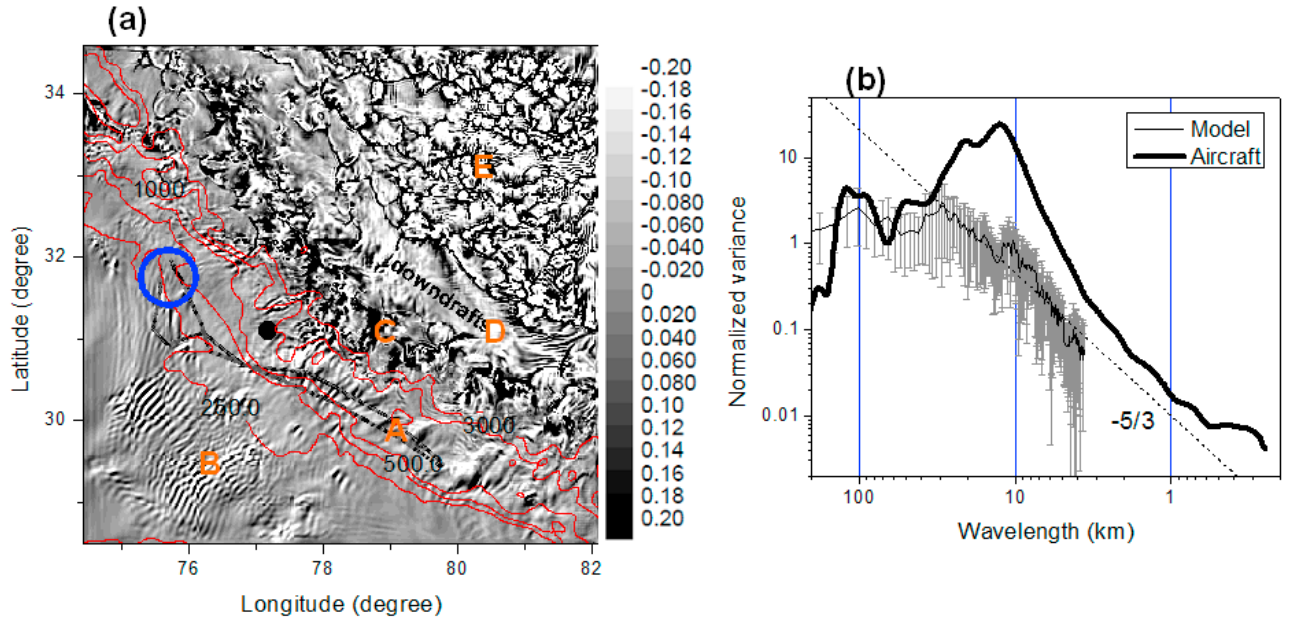

Figure 11. (a) Distribution of model vertical velocity (ms^{-1}) at 6.6 km above mean sea level. Color scale is limited to ± 0.2 ms^{-1}, however maximum updraft is 10 ms^{-1} and maximum downdraft is -4 ms^{-1}. Pathankot airbase location and Mashobra IMD station is also indicated (black dot). (b) A comparison of model and aircraft vertical velocity variance spectra.

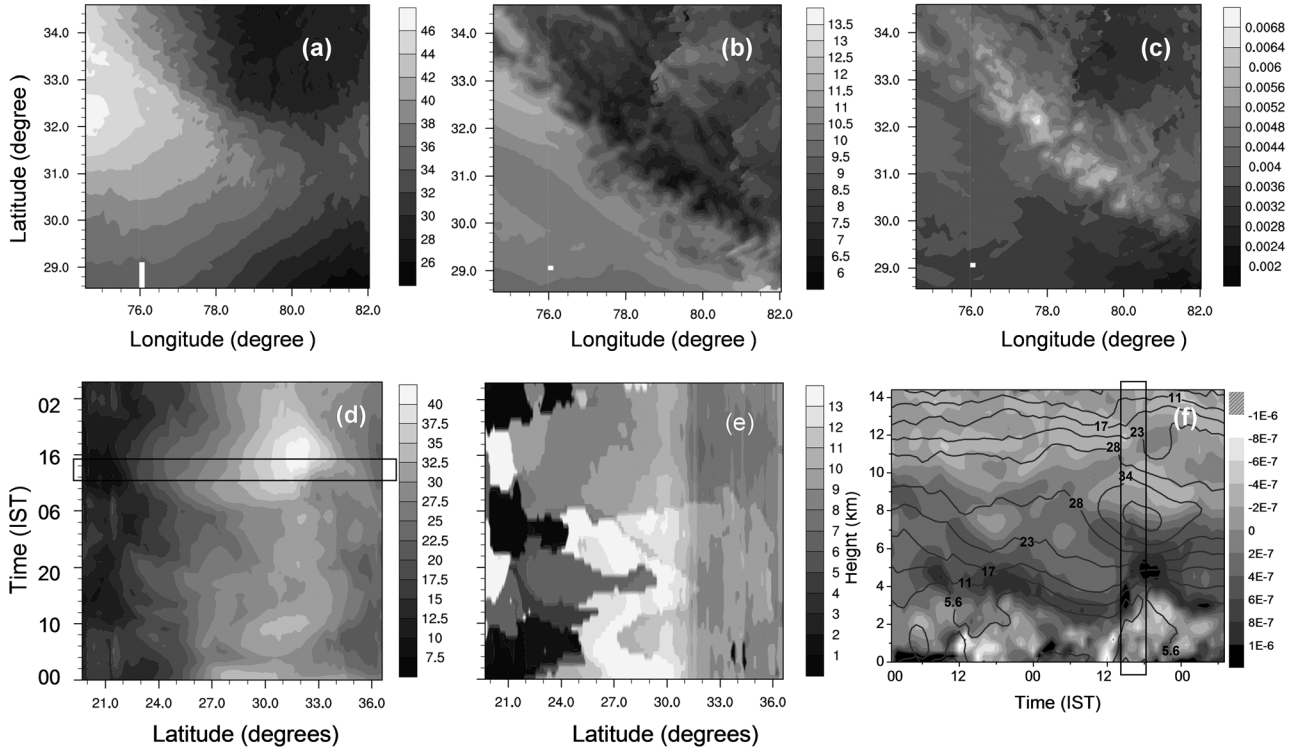

Figure 12. Spatial distribution of (a) jet speed in ms^{-1}, (b) jet height in km, (c) jet shear in units of s^{-1} (ratio of jet and speed and height) during the aircraft observations on 27 May. Latitude and time (beginning from 00 IST on 26 May) variation of (d) jet speed and (e) height from the model. Temporal evolution of vertical component of vorticity (in color) and wind speed (contour) on the summit (Figure 12d).

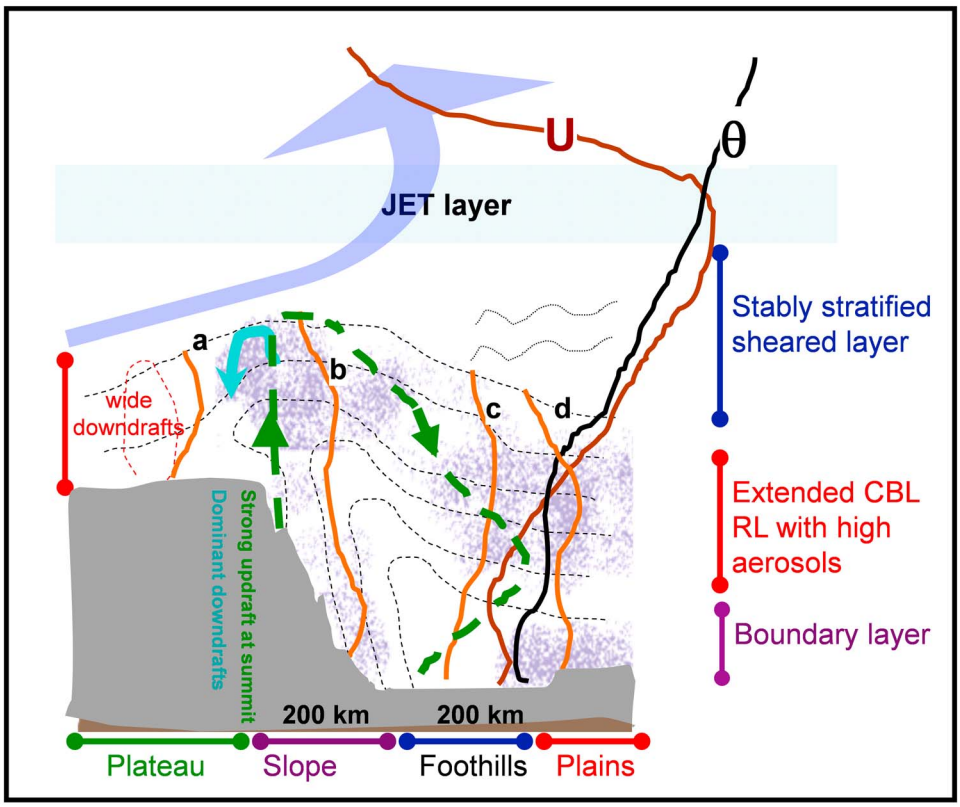

Figure 13. A conceptual model for scale interaction Labels a, b, c, and d show vertical profiles of aerosol attenuation for the conditions over listed regions mentioned in this study for cloud free conditions.

Sarkar [2010] also showed a peak wavelength equal to that of the most unstable mode. In our case this wavelength is 10–12 km, which is attributed to the topographic barrier. This needs further insights from observations and basic simulations to pinpoint the exact cause of the vertical constraining of eddy and the wavelength corresponding to the constrained eddy.

3.3.4. Inference From Flow Visualizations

[40] A three dimensional view of the circulation patterns over the southern slopes of Himalayas is provided at (which is based on a simulation with ARW 3.1 at a resolution of 6 km) http://www.vapor.ucar.edu/images/gallery/TharaHimalayan.png. The visualization of Lagrangian forward trajectories at every 500 km distance (up to 8.5 km) from the surface, originating from the Pathankot air base is shown in the image (light blue color). Trajectory for diurnal cycle (starting at 18 UTC) is presented. The trajectories that originate at lower levels take a course close to the foothills and ascend along the slopes. This behavior is noticed up to 5 km height, indicating stagnating conditions in the boundary layer. Meanwhile three dimensional streamlines for the observation time give a complex flow descent in the valley and a rise over the slopes. The streamlines (color indicates height, red color for heights below 500 m and green color for heights above 6 km, some of the streamlines end at the surface giving the impression of terrain intersection, however those ones indicate the flow stagnation) originating at a lower level takes a course toward the slopes and climbs the slopes at a farther downwind distance (but not directly over the source region). Meanwhile, streamlines that originate at higher elevation would take a horizontal path, very close to the slopes. The upslope transport takes place in complex three dimensional vortices that are situated very close to the slopes. These vortices are oriented in N-S direction. The updrafts are noted along slopes and the descending motion is noticed away from the slopes. Based on the inferences from the observations and numerical simulations conducted in this study, a conceptual understanding of the scale interactions is proposed below.

4. Conceptual View of Dynamical Interactions

[41] A sketch of the dynamical interactions as inferred from various analyses is presented in Figure 13. Four different regions are differentiated in the figure as Plateau, Slope, Foothills, and Plains. The aerosol vertical distribution is presented with single peak over the Plateau (marked a), double peaks on the slopes (marked b), single peak at higher elevation in the Foothills (marked c) and double peak away from the Foothills (marked d). It may be noted that the updraft region is very narrow adhering to the slopes and extend to the plateau. The vertical motions adhering to the topographic barrier brings the surface pollution to higher levels and may also provide pathways for pollution in the elevated layer over the Plains. Several observational findings of higher aerosol concentrations at elevated layers on the slopes from ground based [*Ramana et al.*, 2004; *Hegde et al.*, 2009; *Srivastava et al.*, 2011] and remote sensing [*Gautam et al.*, 2009, 2011; *Brun et al.*, 2011] based studies could be explained with the help of these circulations adhering to the

slopes. *Brun et al.* [2011] also show clear indications of these elevated layers of aerosol slopping over the terrain during night and extending up to 3 km. They also indicate that the possibility of a diurnal cycle in the north south transport of aerosol between the Himalayas and IGP. Some of the earlier works reported possible effect of mountain-valley winds [*Hindman and Upadhyay*, 2002] bringing pollution from the Kathmandu Valley pollution to the surrounding hilltops. However, the cross wind circulations as we report here were not envisioned there. In combination with the residual layer effect over the plains, the elevated layer can be sustained through the cross wind circulations.

[42] Our inferences illustrate that strong jet and its southward extent have a prominent role in the vertical transport as well. However, the strong vertical shear along with strong vertical vorticity may not allow amplification of vertical motions over the plateau. However, in the presence of convective clouds, the low-frequency effects may surpass this containment. A wide subsidence area on the plateau also noted with narrow updraft regions, which may be due to terrain characteristics (the wide valleys and narrow mountains) over the Plateau. As a result, updraft regions are narrow and downdraft regions are wide.

5. Conclusions

[43] For the first time, direct observations of temperature, winds and aerosol concentrations along a horizontal transect over the Indian side of Himalayan slopes are examined. The aircraft observations were carried out over a haze layer at 6.6 km height. The main goal was to investigate scale interactions with the objective of addressing (a) whether there is any evidence of aerosol above the haze layer and (b) what is the source of elevated pollution layer (EPL) away from the slopes. Several repeated features noted in the CALIPSO images such as: an EPL of depth up to 5 km noted farther away from the valley, well mixed conditions with less pollution near the slopes and high pollution 50–100 km away from the slopes, and pockets of high aerosol concentrations over the slopes where there were transport above the haze layer. Specific attention is given to the flow features adjacent to the slopes with a high resolution model. The forced updrafts along southern slopes (both seen in the observations and model) create downdrafts in a region 200 km south of the slopes. However, elevated layers with pollution and deep mixed layers are noticed south of 28°N, which seemed to be a combined effect of the cross wind circulation bringing pollution from the slopes, reservoir of pollution in the residual layer and continuous long range transport from Middle Eastern region below the jet.

[44] Based on the unique observation during CAIPEEX of a horizontal flight with and without clouds across Himalayan slopes, the following main conclusions are drawn.

[45] 1. Aircraft observations of aerosol and CCN indicated dominating fine aerosol along the transect, which also coincided with several fire events along the valley. Fire emissions noted during the study period are found to penetrate deeper layers over the slopes and over the foothills areas. Convective plumes (temperature difference of 1°C) were noted along the horizontal flight tracks at 6.6 km height, which also showed aerosol plumes penetrating the layer above the haze layer.

[46] 2. Aircraft observations of aerosol indicated low concentration adjacent to the slopes and high concentrations away from the slopes which is consistent with CALIPSO observations.

[47] 3. A three-dimensional vertical transfer of energy is noted below the jet, which scaled with the height of the jet of 10–12 km. This indicated presence of a vortex adhering to the slopes. This vortex was also noted in the model simulations.

[48] 4. The presence of clouds along the slopes generated low frequency gravity waves that contributed to the variance in temperature and vertical velocity spectra. Presence of clouds supported amplification of energy at low frequencies.

[49] 5. Meso gamma scale and local scale temperature and vertical velocity variances were comparable to the meso beta scale variance in the vicinity and within cloud passes.

[50] 6. Results of the CAIPEEX observations and the numerical modeling support the vertical exchange of heat and aerosol taking place in localized regions along the slopes and the north-south oriented circulation responsible for the buildup of aerosol at elevated layers along with the residual layer effect in the plains.

[51] 7. Though the numerical model was able to represent the $-5/3$ slope in the velocity spectra, the small scale energy was underestimated by the model.

[52] 8. Examination of model vertical velocity field during the aircraft observations showed presence of strong updraft region along the slopes, gravity wave generation below the jet, in the stably stratified and strongly sheared layer.

[53] 9. Lifting of pollution above the haze layer was found both in the observations and model, in the presence of strong updrafts, which seem to be taking place over selected localized regions and not as large scale lifting along the slope.

[54] The trajectory analysis (forward trajectories are computed with the help of ARW model outputs of three dimensional wind components) from the ARW model supports the idea that the complex three-dimensional vortices are tilted and lie close to the slopes. A trajectory originating very close to the slopes adheres to these vortices.

[55] On the large scale the 'Tibetan Plateau generates significant diurnally varying circulations, vertical motion, and diabatic heating features [*Luo and Yanai*, 1983; *Nitta*, 1983; *Krishnamurti and Kishtawal*, 2000]. Spatial structure of the circulations at scales larger than 100 km over Himalayan region were studied in relationship with monsoon circulations [*Murakami*, 1987] (also several references in *Molnar et al.* [2010]) earlier, however there has been insufficient information at smaller scales. CAIPEEX observations give a first time glimpse of such information. Specially designed flights need to be planned to document the characteristics of the crosswind circulations and their boundary layer interaction, which is crucial for further understanding of the elevated pollution layer. However, year 2009 was one of the drought years and several concurrent experiments (CAIPEEX, JAMEX, etc.) have taken place near the Himalayan region, a combination of such observational and simulation efforts to address the important science questions such as the exchange between the IGV and Tibetan Plateau could be explored further. Our study has limited data sets and focused campaigns in similar situations

are necessary to establish the impact of these findings over a wider scale.

[56] There are increasing evidences of enhanced warming, early snowmelt, and retreat of high mountain glaciers in the Himalayas and the Tibetan Plateau [*IPCC*, 2007]. Particularly in the western and central Himalayas, the rate of retreat has been increasing in the recent decades [*Raina and Sangewar*, 2007; *Jain*, 2008]. This information imposes significant stress on the hydrological cycle and the fresh water supply [*Kehrwald et al.*, 2008]. Thus the region of investigation is quite vulnerable and further detailed investigations with the help of high resolution simulations are needed.

[57] **Acknowledgments.** Indian Institute of Tropical Meteorology (IITM) and the CAIPEEX experiment is fully funded by Ministry of Earth Sciences, Government of India, New Delhi. We thank all the CAIPEEX team members. We thank CALIPSO, MODIS and AERONET teams for their respective data. We also thank P. Kulkarni and G. Urankar for preparation of some data sets. We acknowledge three anonymous, excellent reviews on this manuscript, which helped improve this manuscript immensely. We also acknowledge critical suggestions from Editor Steven Ghan.

References

Attié, J.-L., and P. Durand (2003), Conditional wavelet technique applied to aircraft data measured in the thermal internal boundary layer during seabreeze events, *Boundary Layer Meteorol.*, *106*(3), 359–382, doi:10.1023/A:1021262406408.

Barros, A. P., G. Kim, E. Williams, and S. W. Nesbitt (2004), Probing orographic controls in the Himalayas during the monsoon using satellite imagery, *Nat. Hazards Earth Syst. Sci.*, *4*, 29–51, doi:10.5194/nhess-4-29-2004.

Brun, J., P. Shrestha, and A. P. Barros (2011), Mapping aerosol intrusion in Himalayan valleys using the Moderate Resolution Imaging Spectroradiometer (MODIS) and Cloud Aerosol Lidar and Infrared Pathfinder Satellite Observation (CALIPSO), *Atmos. Environ.*, *45*, 6382–6392, doi:10.1016/j.atmosenv.2011.08.026.

Carrico, C. M., M. H. Bergin, A. B. Shrestha, J. E. Dibb, L. Gomes, and J. M. Harris (2003), The importance of carbon and mineral dust to seasonal aerosol properties in the Nepal Himalaya, *Atmos. Environ.*, *37*, 2811–2824.

Chakraborty, A., R. S. Nanjundiah, and J. Srinivasan (2006), Theoretical aspects of the onset of Indian summer monsoon from perturbed orography simulations in a GCM, *Ann. Geophys.*, *24*, 2075–2089, doi:10.5194/angeo-24-2075-2006.

Chan, C. Y., et al. (2003), Characteristic of biomass burning emission sources, transport, and chemical speciation in enhanced springtime tropospheric ozone profile over Hong Kong, *J. Geophys. Res.*, *108*(D1), 4015, doi:10.1029/2001JD001555.

Chen, F., and J. Dudhia (2001), Coupling an advanced land surface–hydrology model with the Penn State–NCAR MM5 modeling system. Part I: Model implementation and sensitivity, *Mon. Weather Rev.*, *129*, 569–585.

Cornish, C. R., C. S. Bretherton, and D. B. Percival (2006), Maximal overlap wavelet statistical analysis with application to atmospheric turbulence, *Boundary Layer Meteorol.*, *119*(2), 339–374, doi:10.1007/s10546-005-9011-y.

Cuxart, J., et al. (2000), Stable boundary layer experiment in Spain (SABLES-98), A report, *Boundary Layer Meteorol.*, *96*, 337–370, doi:10.1023/A:1002609509707.

Daubechies, I. (1991), *Ten Lectures on Wavelets*, SIAM, Philadelphia, Pa.

Decesari, S., et al. (2010), Chemical composition of PM10 and PM1 at the high-altitude Himalayan station Nepal Climate Observatory-Pyramid (NCO-P) (5079 m a.s.l.), *Atmos. Chem. Phys.*, *10*, 4583–4596, doi:10.5194/acp-10-4583-2010.

Farge, M. (1992), Wavelet transforms and their applications to turbulence, *Annu. Rev. Fluid Mech.*, *24*, 395–458, doi:10.1146/annurev.fl.24.010192.002143.

Folkins, A. R., D. Chatfield, D. Baumgardner, and D. Proffitt (1997), Biomass burning and deep convection in southeastern Asia: Results from ASHOE/MAESA, *J. Geophys. Res.*, *102*, 13,291–13,299, doi:10.1029/96JD03711.

Galmarini, S., and J. L. Attié (2000), Turbulent transport at the thermal internal boundary-layer top: Wavelet analysis of aircraft measurements, *Boundary Layer Meteorol.*, *94*(2), 175–196, doi:10.1023/A:1002498707645.

Gamo, M. (1996), Thickness of the dry convection and large-scale subsidence above deserts, *Boundary Layer Meteorol.*, *79*, 265–278, doi:10.1007/BF00119441.

Gautam, R., N. C. Hsu, K. M. Lau, S. C. Tsay, and M. Kafatos (2009), Enhanced pre-monsoon warming over the Himalayan-Gangetic region from 1979 to 2007, *Geophys. Res. Lett.*, *36*, L07704, doi:10.1029/2009GL037641.

Gautam, R., et al. (2011), Accumulation of aerosol over the Indo-Gangetic plains and southern slopes of the Himalayas: Distribution, properties and radiative effects during the 2009 pre-monsoon season, *Atmos. Chem. Phys.*, *11*, 12,841–12,863, doi:10.5194/acp-11-12841-2011.

Grossmann, A., and J. Morlet (1984), Decomposition of Hardy functions into square integrable wavelets of constant shape, *SIAM J. Math. Anal.*, *15*, 723–736, doi:10.1137/0515056.

Hahn, D. G., and S. Manabe (1975), The role of mountains in the south Asian monsoon circulation, *J. Atmos. Sci.*, *32*, 1515–1541, doi:10.1175/1520-0469(1975)032<1515:TROMIT>2.0.CO;2.

Hegde, P., P. Pant, and Y. Bhavanikumar (2009), An integrated analysis of lidar observations in association with optical properties of aerosol from a high altitude location in central Himalayas, *Atmos. Sci. Lett.*, *10*, 48–57, doi:10.1002/asl.209.

Hindman, E. E., and B. P. Upadhyay (2002), Air pollution transport in the Himalayas of Nepal and Tibet during the 1995–1996 dry season, *Atmos. Environ.*, *36*, 727–739, doi:10.1016/S1352-2310(01)00495-2.

Hong, S.-Y., Y. Noh, and J. Dudhia (2006), A new vertical diffusion package with an explicit treatment of entrainment processes, *Mon. Weather Rev.*, *134*, 2318–2341, doi:10.1175/MWR3199.1.

Houze, R. A., Jr., D. C. Wilton, and B. F. Smull (2007), Monsoon convection in the Himalayan region as seen by the TRMM Precipitation radar, *Q. J. R. Meteorol. Soc.*, *133*, 1389–1411, doi:10.1002/qj.106.

Huang, Q., J. H. Marsham, D. J. Parker, W. Tian, and C. M. Grams (2010), Simulations of the effects of surface heat flux anomalies on stratification, convective growth, and vertical transport within the Saharan boundary layer, *J. Geophys. Res.*, *115*, D05201, doi:10.1029/2009JD012689.

Hunt, J. C. R., and P. A. Durbin (1999), Perturbed vortical layers and shear sheltering, *Fluid Dyn. Res.*, *24*, 375–404, doi:10.1016/S0169-5983(99)00009-X.

Intergovernmental Panel on Climate Change (2007), *Climate Change 2007: The Physical Science Basis. Contribution of Working Group I to the Fourth Assessment Report of the Intergovernmental Panel on Climate Change*, edited by S. Solomon et al., Cambridge Univ. Press, Cambridge, U. K.

Jain, S. K. (2008), Impact of retreat of Gangotri glacier on the flow of Ganga River, *Curr. Sci.*, *95*, 1012–1014.

Kehrwald, N. M., L. G. Thompson, Y. Tandong, E. Mosley-Thompson, U. Schotterer, V. Alfimov, J. Beer, J. Eikenberg, and M. E. Davis (2008), Mass loss on Himalayan glacier endangers water resources, *Geophys. Res. Lett.*, *35*, L22503, doi:10.1029/2008GL035556.

Krishnamurti, T. N., and C. M. Kishtawal (2000), A pronounced continental-scale diurnal mode of the Asian summer monsoon, *Mon. Weather Rev.*, *128*, 462–473, doi:10.1175/1520-0493(2000)128<0462:APCSDM>2.0.CO;2.

Kuhlmann, J., and J. Quaas (2010), How can aerosol affect the Asian summer monsoon? Assessment during three consecutive pre-monsoon seasons from CALIPSO satellite data, *Atmos. Chem. Phys.*, *10*, 4673–4688, doi:10.5194/acp-10-4673-2010.

Kulkarni, J. R., et al. (2012), The Cloud Aerosol Interactions and Precipitation Enhancement Experiment (CAIPEEX): Overview and preliminary results, *Curr. Sci.*, *102*(3), 413–425.

Lau, K.-M., and K.-M. Kim (2006), Observational relationships between aerosol and Asian monsoon rainfall, and circulation, *Geophys. Res. Lett.*, *33*, L21810, doi:10.1029/2006GL027546.

Lau, K.-M., M.-K. Kim, and K.-M. Kim (2006), Asian monsoon anomalies induced by aerosol direct forcing: The role of the Tibetan Plateau, *Clim. Dyn.*, *26*, 855–864.

Lau, K.-M., et al. (2008), The joint aerosol-monsoon experiment: A new challenge for monsoon climate research, *Bull. Am. Meteorol. Soc.*, *89*, 369–383, doi:10.1175/BAMS-89-3-369.

Lau, W. K. M., M.-K. Kim, K.-M. Kim, and W.-S. Lee (2010), Enhanced surface warming and accelerated snow melt in the Himalayas and Tibetan Plateau induced by absorbing aerosols, *Environ. Res. Lett.*, *5*(2), 025204, doi:10.1088/1748-9326/5/2/025204.

Lilly, D. K. (1983), Stratified turbulence and the mesoscale variability of the atmosphere, *J. Atmos. Sci.*, *40*, 749–761, doi:10.1175/1520-0469(1983)040<0749:STATMV>2.0.CO;2.

Lim, K.-S. S., and S.-Y. Hong (2010), Development of an effective double-moment cloud microphysics scheme with prognostic cloud condensation nuclei (CCN) for weather and climate models, *Mon. Weather Rev.*, *138*, 1587–1612, doi:10.1175/2009MWR2968.1.

Liu, X., A. Bai, and C. Liu (2009), Diurnal variations of summertime precipitation over the Tibetan Plateau in relation to orographically induced regional circulations, *Environ. Res. Lett.*, *4*, 045203, doi:10.1088/1748-9326/4/4/045203.

Liu, Z., et al. (2008), Airborne dust distributions over the Tibetan Plateau and surrounding areas derived from the first year of CALIPSO lidar observations, *Atmos. Chem. Phys. Discuss.*, *8*, 5040–5060.

Luo, H., and M. Yanai (1983), The large-scale circulation and heat sources over the Tibetan Plateau and surrounding areas during the early summer of 1979. Part I: Precipitation and kinematic analysis, *Mon. Weather Rev.*, *111*, 922–944.

Luo, H., and M. Yanai (1984), The large-scale circulation and heat sources over the Tibetan Plateau and surrounding areas during the early summer of 1979. Part II: Heat and moisture budgets, *Mon. Weather Rev.*, *112*, 966–989, doi:10.1175/1520-0493(1984)112<0966:TLSCAH>2.0.CO;2.

Ma, Y., S. Fan, H. Ishikawa, O. Tsukamoto, T. Yao, T. Koike, H. Zuo, Z. Hu, and Z. Su (2005), Diurnal and inter-monthly variation of land surface heat fluxes over the central Tibetan Plateau area, *Theor. Appl. Climatol.*, *80*, 259–273, doi:10.1007/s00704-004-0104-1.

Meyers, S. D., B. G. Kelly, and J. J. O'Brien (1993), An introduction to wavelet analysis in oceanography and meteorology: With application to the dispersion of the Yanai waves, *Mon. Weather Rev.*, *121*, 2858–2866, doi:10.1175/1520-0493(1993)121<2858:AITWAI>2.0.CO;2.

Molnar, P., W. R. Boos, and D. S. Battisti (2010), Orographic controls on climate and paleoclimate of Asia: Thermal and mechanical roles for the Tibetan Plateau, *Annu. Rev. Earth Planet. Sci.*, *38*, 77–102, doi:10.1146/annurev-earth-040809-152456.

Murakami, T. (1987), *Effects of the Tibetan Plateau: Monsoon Meteorology*, edited by C. P. Chang and T. N. Krishnamurty, Oxford Univ. Press, Oxford, U. K.

Nitta, T. (1983), Observational study of heat sources over the eastern Tibetan Plateau during the summer monsoon, *J. Meteorol. Soc. Jpn.*, *61*, 590–605.

Pham, T. H., and S. Sarkar (2010), Internal waves and turbulence in a stable stratified jet, *J. Fluid Mech.*, *648*, 297–324, doi:10.1017/S0022112009993120.

Prabha, T., M. Leclerc, A. Karipot, D. Hollinger, and E. Mursch-Radlgruber (2008), Influence of nocturnal low-level jets on eddy-covariance fluxes over a tall forest canopy, *Boundary Layer Meteorol.*, *126*(2), 219–236, doi:10.1007/s10546-007-9232-3.

Prabha, T. V., A. Khain, R. S. Maheshkumar, G. Pandithurai, J. R. Kulkarni, M. Konwar, and B. N. Goswami (2011), Microphysics of pre-monsoon and monsoon clouds as seen from in situ measurements during CAIPEEX, *J. Atmos. Sci.*, *68*(9), 1882–1901, doi:10.1175/2011JAS3707.1.

Prasad, A. K., K. H. S. Yang, H. M. El-Askary, and M. Kafatos (2009), Melting of major glaciers in the western Himalayas: Evidence of climatic changes from long term MSU derived tropospheric temperature trend (1979–2008), *Ann. Geophys.*, *27*, 4505–4519, doi:10.5194/angeo-27-4505-2009.

Raina, V. K., and C. Sangewar (2007), Siachen glacier of Karakorum Mountains, Ladakh, its secular retreat, *J. Geol. Soc. India*, *70*, 11–16.

Raj, P. E., S. K. Saha, S. M. Sonbawne, S. M. Desphpande, P. C. S. Devara, Y. Rao Jaya, K. K. Dani, and G. Pandithurai (2008), Lidar observation of aerosol stratification in the lower troposphere over Pune during pre-monsoon season of 2006, *Proc. Indian Acad. Sci., Earth Planet. Sci.*, *117*, 293–302.

Ramana, M. V., V. Ramanathan, I. A. Podgorny, B. B. Pradhan, and B. Shrestha (2004), The direct observations of large aerosol radiative forcing in the Himalayan region, *Geophys. Res. Lett.*, *31*, L05111, doi:10.1029/2003GL018824.

Ramanathan, V., and P. J. Crutzen (2003), New directions: Atmospheric brown clouds, *Atmos. Environ.*, *37*, 4033–4035, doi:10.1016/S1352-2310(03)00536-3.

Ramanathan, V., C. Chung, D. Kim, T. Bettge, L. Buja, J. T. Kiehl, W. M. Washington, Q. Fu, D. R. Sikka, and M. Wild (2005), Atmospheric brown clouds: Impact on South Asian climate and hydrologic cycle, *Proc. Natl. Acad. Sci. U. S. A.*, *102*, 5326–5333, doi:10.1073/pnas.0500656102.

Reddy, M. S., and C. Venkataraman (2002a), Inventory of aerosol and sulfur dioxide emissions from India: I. Fossil fuel combustion, *Atmos. Environ.*, *36*, 677–697, doi:10.1016/S1352-2310(01)00463-0.

Reddy, M. S., and C. Venkataraman (2002b), Inventory of aerosol and sulfur dioxide emissions from India: II. Biomass combustion, *Atmos. Environ.*, *36*, 699–712, doi:10.1016/S1352-2310(01)00464-2.

Satheesh, S. K., K. Krishna Moorthy, S. Suresh Babu, V. Vinoj, and C. B. S. Dutt (2008), Climate implications of large warming by elevated aerosol over India, *Geophys. Res. Lett.*, *35*, L19809, doi:10.1029/2008GL034944.

Shrestha, A. B., C. P. Wake, J. E. Dibb, P. A. Mayewski, S. I. Whitlow, G. R. Carmichael, and M. Ferm (2000), Seasonal variations in aerosol concentrations and compositions in the Nepal Himalaya, *Atmos. Environ.*, *34*, 3349–3363, doi:10.1016/S1352-2310(99)00366-0.

Shrestha, A. B., C. P. Wake, J. E. Dibb, and S. I. Whitlow (2002), Aerosol and precipitation chemistry at a remote Himalayan site in Nepal, *Aerosol Sci. Technol.*, *36*, 441–456, doi:10.1080/027868202753571269.

Shrestha, P., and A. P. Barros (2010), Joint spatial variability of aerosol, clouds and rainfall in the Himalayas from satellite data, *Atmos. Chem. Phys.*, *10*, 8305–8317, doi:10.5194/acp-10-8305-2010.

Shrestha, P., A. P. Barros, and A. Khlystov (2010), Chemical composition and aerosol size distribution of the middle mountain range in the Nepal Himalayas during the 2009 pre-monsoon season, *Atmos. Chem. Phys.*, *10*, 11,605–11,621, doi:10.5194/acp-10-11605-2010.

Smedman, A. S., U. Högström, and J. C. R. Hunt (2004), Effects of shear-sheltering in a stable atmospheric boundary-layer with strong shear, *Q. J. R. Meteorol. Soc.*, *130*, 31–50, doi:10.1256/qj.03.68.

Srivastava, A. K., P. Pant, P. Hegde, S. Singh, U. C. Dumka, M. Naja, N. Singh, and Y. Bhavanikumar (2011), Influence of a south Asian dust storm on aerosol radiative forcing at a high-altitude station in central Himalayas, *Int. J. Remote Sens.*, *32*, 7827–7845, doi:10.1080/01431161.2010.531781.

Srivastava, A. K., K. Ram P. Pant, P. Hegde, and H. Joshi (2012), Black carbon aerosols over Manora Peak in the Indian Himalayan foothills: Implications for climate forcing, *Environ. Res. Lett.*, *7*, 014002, doi:10.1088/1748-9326/7/1/014002.

Stone, E. A., J. J. Schauer, B. B. Pradhan, P. M. Dangol, G. Habib, C. Venkataraman, and V. Ramanathan (2010), Characterization of emissions from South Asian biofuels and application to source apportionment of carbonaceous aerosol in the Himalayas, *J. Geophys. Res.*, *115*, D06301, doi:10.1029/2009JD011881.

Terradellas, E., G. Morales, J. Cuxart, and C. Yagüe (2001), Wavelet methods: Application to the study of the stable atmospheric boundary-layer under non-stationary conditions, *Dyn. Atmos. Oceans*, *34*, 225–244, doi:10.1016/S0377-0265(01)00069-0.

Thomas, C., and T. Foken (2007), Organized motion in a tall spruce canopy: Temporal scales, structure spacing and terrain effects, *Boundary Layer Meteorol.*, *122*(1), 123–147, doi:10.1007/s10546-006-9087-z.

Vadrevu, K. P., E. Ellicott, L. Giglio, K. V. S. Badarinath, E. Vermote, C. Justice, and W. K. M. Lau (2012), Vegetation fires in the Himalayan region: Aerosol load, black carbon emissions and smoke plume heights, *Atmos. Environ.*, *47*, 241–251, doi:10.1016/j.atmosenv.2011.11.009.

Wu, G.-X., et al. (2007), The influence of mechanical and thermal forcing by the Tibetan Plateau on Asian climate, *J. Hydrometeorol.*, *8*, 770–789, doi:10.1175/JHM609.1.

Xavier, P. K., and B. N. Goswami (2007), A promising alternative to prediction of seasonal mean all India rainfall, *Curr. Sci.*, *93*, 195–202.

Yanai, M., and G.-X. Wu (2006), Effects of the Tibetan Plateau, in *The Asian Monsoon*, edited by B. Wang, pp. 513–549, Springer, Berlin.